

# Direct numerical simulation of vortex synchronization due to small perturbations

S. H. KIM<sup>1</sup>, J. Y. PARK<sup>2</sup>, N. PARK<sup>3</sup>, J. H. BAE<sup>4</sup>  
AND J. Y. YOO<sup>1,5†</sup>

<sup>1</sup>School of Mechanical and Aerospace Engineering, Seoul National University, Seoul 151-744, Korea

<sup>2</sup>Halla Climate Control Corporation, Daejeon 306-230, Korea

<sup>3</sup>Department of Aerospace Engineering and Mechanics, University of Minnesota, Minneapolis, MN 55455, USA

<sup>4</sup>Mechanical and Aerospace Engineering Department, University of California, Los Angeles, CA 90095-1597, USA

<sup>5</sup>Institute of Advanced Machinery and Design, Seoul National University, Seoul 151-744, Korea

(Received 3 September 2007 and in revised form 12 March 2009)

Direct numerical simulation (DNS) is performed to investigate the vortex synchronization phenomena in the wake behind a circular cylinder at the Reynolds numbers,  $Re = 220$  (mode-A regime) and 360 (mode-B regime). To generate vortex synchronization, a sinusoidal streamwise velocity perturbation, the frequency of which is about twice the natural shedding frequency, is superimposed on the free stream velocity. At  $Re = 360$ , vortex synchronization occurs when the perturbation frequency is exactly twice the natural shedding frequency. However, at  $Re = 220$ , it does not occur when the same perturbation frequency condition is imposed. Instead, it occurs when the perturbation frequency is near twice the hypothetical two-dimensional laminar vortex shedding frequency as if there were no wake transition at  $Re = 220$ .

It is elucidated that, as a result of vortex synchronization, the trajectory of the Kármán vortices and the vortex structure are changed. The Kármán vortices are formed along the mean separating streamline slightly inside the mean wake bubble at  $Re = 220$ , but slightly outside at  $Re = 360$ . Thus, the Reynolds shear stress force has different contribution to the streamwise force balance of the mean wake bubble depending on the Reynolds numbers: its magnitude is negligible at  $Re = 220$ , compared to other force components, while it reverses its sign at  $Re = 360$ . More importantly, at  $Re = 220$ , the mode-A instability is suppressed into two-dimensional laminar flow with strong Kármán vortices. At  $Re = 360$ , the dominant instability mode changes from mode B to mode A.

---

## 1. Introduction

The wake behind a circular cylinder has been investigated for so many years because of its importance in fluid mechanics. In particular, this flow can be characterized by one single parameter, the Reynolds number ( $Re$ ), based on the cylinder diameter ( $D$ ). Near  $Re = 49$ , the Kármán vortex alley is formed with periodic shedding of vortices. This two-dimensional laminar flow becomes three-dimensional with the start of wake transition. According to Williamson (1996*b*), the wake transition involves two

† Email address for correspondence: jyyoo@snu.ac.kr

discontinuous changes which can be represented with small-scale three-dimensional instability modes (i.e. modes A and B). For the first discontinuity around  $Re = 180$ – $194$ , which is hysteric, the Strouhal number ( $St$ ) drops down abruptly from the value on the extension of the laminar flow curve with the onset of streamwise vortex pairs (mode A) of which the spanwise wavelength is approximately 3–4 cylinder diameters. This mode-A instability is generated due to wavy deformation of the Kármán vortices as they are shed. As  $Re$  increases up to 230–260,  $St$  jumps up gradually with the emergence of mode-B instability which becomes more dominant than mode-A instability. The streamwise vortex pairs for mode B are not related with the deformation of Kármán vortices, but originated from an instability in the braid shear layer region, which have finer spanwise wavelength of about 1 cylinder diameter ( $1D$ ). Since two transition modes have different characteristics and physical origins as Williamson (1996*b*) pointed out, many researches have been performed to investigate these wake transition modes for unperturbed flow (natural shedding state) by Zhang, Fey & Noack (1995), Brede, Eckelmann & Rockwell (1996), Henderson (1997), Persillon & Braza (1998), etc.

In the meanwhile, it is considered that when a bluff body is excited by an external force, the vortex shedding frequency may be synchronized with the external forcing frequency. This resonance is commonly termed vortex lock-on or vortex synchronization which can occur with various external forcings such as in-line, or transverse, or rotational oscillation of a cylinder, or an oscillatory incident flow. According to an extensive review of Griffin & Hall (1991), for the transverse and rotational oscillation cases, the vortex shedding frequency is synchronized with the oscillation frequency ( $f_p$ ) when it is near the natural shedding frequency ( $f_n$ ). On the other hand, in the case of the oscillatory incident flow or in-line oscillation of a circular cylinder, vortex synchronization occurs when  $f_p$  is near twice  $f_n$ . When vortex synchronization takes place, there is a substantial increase not only in the mean drag but also in the oscillatory drag and lift forces. Since these increased forces may cause structural vibrations and acoustic noises, and in some cases trigger failure, vortex synchronization can impose serious problems in many engineering applications (Griffin & Hall 1991).

In the case of oscillatory incident flow, Konstantinidis, Balabani & Yianneskis (2003) presented a parametric map, which shows the limit of the vortex synchronization regime in terms of perturbation amplitude and frequency. They used their own experimental data and previously published data obtained in the range of Reynolds numbers  $80 \leq Re \leq 40\,000$ , where the trough of the vortex synchronization regime (defined by the minimum amplitude that can generate vortex synchronization) is generally shown to be formed near the point corresponding to twice  $f_n$ . However, the vortex synchronization regime obtained by Griffin & Ramberg (1976) at  $Re = 190$  seems to show that the trough is shifted somewhat towards the point corresponding to more than twice  $f_n$ . We paid our attention to this different trends in the vortex synchronization regime for the particular Reynolds number belonging to mode-A regime, which has not been explained clearly yet.

In order to compare the vortex dynamics between the natural shedding and vortex synchronization states, Kim, Yoo & Sung (2006) investigated the trajectory of the vortex centre and the streamwise force balance for the mean wake bubble at  $Re = 360$  (mode-B regime) using the data obtained by time-resolved particle image velocimetry (PIV) technique. The streamwise force balance for the mean wake bubble, which was considered by Roshko (1993) and extended for various wake flows by Balachandar, Mittal & Najjar (1997), is maintained between the net Reynolds stresses and the

pressure forces acting on the boundary of the mean wake bubble. They also showed that the direction of the net Reynolds shear stress force was reversed due to the occurrence of vortex synchronization. This reversal was explained by examining the trajectory of the vortex centre. That is, in the natural shedding state the vortex centre was formed inside the mean wake bubble, while in the vortex synchronization state it was formed outside. Their interpretation of vortex dynamics for the vortex synchronization state at mode-B regime has motivated us to start the present study on the vortex synchronization state at mode-A regime, because the wake flows for mode-A and mode-B regimes might show different characteristics in the vortex synchronization states due to their different physical origins.

In the present study, we focus on the vortex synchronization phenomena in the circular cylinder wakes at  $Re = 220$  (mode-A regime) and 360 (mode-B regime) by using direct numerical simulation (DNS). First, the conditions of perturbation frequency required for the occurrence of vortex synchronization are examined at each  $Re$ . From this, we discuss the reason why the shape of the vortex synchronization regime at the particular  $Re$  is different from that of the general vortex synchronization regime. Second, as an extension of Kim *et al.* (2006), we investigate the changes in the trajectory of the vortex centre and its effects on the streamwise force balance for the mean wake bubble in the vortex synchronization state. For a direct comparison with Kim *et al.* (2006), we are to adopt the same notations and the same logic. Finally, the vortex structures in the vortex synchronization state are compared with those in the natural shedding state. In particular, comparing the streamwise vorticity components in the wake region, the characteristics of the streamwise vortex pairs are investigated, which are changed due to the occurrence of vortex synchronization. The physical mechanism of this change is explained by analysing the formation of the saddle point in the braid shear layer.

## 2. Numerical details

In this section, an outline of direct numerical simulation is described, including the governing equations, numerical method, boundary conditions and grid system.

The governing equations used in the present study are based on the compressible flow formulation of the Navier–Stokes equations. In the Cartesian coordinate system, they take the following form:

$$\begin{aligned} \frac{\partial \rho}{\partial t} + \frac{\partial \rho u_k}{\partial x_k} &= 0, \\ \frac{\partial \rho u_i}{\partial t} + \frac{\partial}{\partial x_k} (\rho u_i u_k + p \delta_{ik} - \sigma_{ik}) &= 0, \\ \frac{\partial E_T}{\partial t} + \frac{\partial}{\partial x_k} \{(E_T + p) u_k - \sigma_{ik} u_i - Q_k\} &= 0, \end{aligned} \quad (2.1)$$

where  $\rho$  is the density,  $(u_1, u_2, u_3) = (u, v, w)$  is the velocity vector,  $E_T$  is the total energy,  $p$  is the pressure given by the relationship  $p = (\gamma - 1)(E_T - \rho u_k u_k / 2)$ ,  $\gamma = 1.4$  is the specific heat ratio and  $\delta_{ik}$  is the Kronecker delta. After appropriate non-dimensionalization, the stress tensor  $\sigma_{ik}$  and the heat flux vector  $Q_k$  are given by

$$\begin{aligned} \sigma_{ik} &= \frac{\mu}{Re} \left( \frac{\partial u_i}{\partial x_k} + \frac{\partial u_k}{\partial x_i} - \frac{2}{3} \frac{\partial u_l}{\partial x_l} \delta_{ik} \right), \\ Q_k &= \frac{\mu}{(\gamma - 1) M^2 Re Pr} \frac{\partial T}{\partial x_k}, \end{aligned} \quad (2.2)$$

where  $T$  is the temperature and the Reynolds number  $Re = \rho_\infty U_\infty D / \mu_\infty$  is defined in terms of the free stream velocity  $U_\infty$  and the cylinder diameter  $D$  (subscript  $\infty$  denotes far-field values);  $M = U_\infty / \sqrt{\gamma RT_\infty}$  and  $Pr = \mu C_p / k$  are the free stream Mach number and the Prandtl number, where  $R$ ,  $C_p$  and  $k$  are gas constant, constant pressure specific heat and thermal conductivity, respectively. In this study, we assume that  $M = 0.2$  and  $Pr = 0.7$ , which correspond to subsonic condition of the air.

Although practically incompressible flows are considered, compressible flow formulation is adopted because (i) it naturally enables us to use high-resolution schemes on a structured mesh, and (ii) it also constitutes the basis for direct computation of flow-induced noise and heat transfer in the future work. Computational overhead caused by using compressible solver for low-Mach-number flow is compensated with high-resolution discretization and implicit time-marching scheme, as will be described below.

In order to handle the cylinder geometry, governing equations (2.1) are translated to the form in curvilinear coordinates. To overcome severe limitation on computational time step, fully implicit second-order Crank–Nicolson scheme is adopted and the fourth-order compact difference scheme (Lele 1992; Ekaterinaris 1999; Park, Yoo & Choi 2004) is used for all spatial derivatives including metric terms. For minimization of the aliasing error, nonlinear terms are written in skew-symmetric form (Park *et al.* 2004). In order to avoid the degradation of modified wavenumber characteristics, hybrid collocated and staggered grid system (Lele 1992; Nagarajan, Lele & Ferziger 2003) is adopted in the sense that conservative variables and convective flux vectors are defined at grid points while viscous flux vectors are defined at staggered positions. An eighth-order compact filter (Lele 1992; Visbal & Gaitonde 1999) is applied to the computational variables at every twentieth time steps to damp out numerical instabilities originated from odd–even decoupling, mesh non-uniformity and boundary conditions. More detailed explanation of the numerical method are provided in the Appendix.

Figure 1 shows the schematics of computational domain and boundary conditions, and an O-type grid near the wake region. Treatment of boundary conditions is similar to that of Beaudan & Moin (1994). On the cylinder surface, no-slip and adiabatic conditions are imposed. The outer circular boundary is divided into three parts, i.e. inflow, outflow and wake boundaries, as illustrated in figure 1(a). On the inflow and outflow boundaries, classical method of characteristics is applied to the flow variables. Thus, the inflow boundary conditions are expressed as

$$\frac{p}{\rho^\gamma} = \left( \frac{p}{\rho^\gamma} \right)_\infty, \quad R_1 = R_{1\infty}, \quad \partial_\eta R_2 = 0, \quad V_T = V_{T\infty}, \quad w = 0, \quad (2.3)$$

where  $R_1 = V_N + 2c/(\gamma - 1)$ ,  $R_2 = V_N - 2c/(\gamma - 1)$ ,  $V_N = (-\eta_x u - \eta_y v) / \sqrt{\eta_x^2 + \eta_y^2}$ , and  $V_T = (\eta_y u - \eta_x v) / \sqrt{\eta_x^2 + \eta_y^2}$  are the first and second Riemann invariants, the normal and tangential components of the velocity, respectively, and  $\eta_x$  and  $\eta_y$  are the metric terms. As the counterpart of (2.3), the outflow conditions are given by

$$\partial_\eta \left( \frac{p}{\rho^\gamma} \right) = 0, \quad \partial_\eta V_T = 0, \quad \partial_\eta R_1 = 0, \quad R_2 = R_{2\infty}, \quad \partial_\eta w = 0. \quad (2.4)$$

On the wake boundary, Neumann condition  $\partial_\eta \mathbf{q} = 0$  is applied to all conservative variables, where  $\mathbf{q} = J^{-1}[\rho, \rho u, \rho v, \rho w, E_T]^T$  is the solution vector,  $J$  is the Jacobian of the coordinate transformation. Periodic boundary condition is imposed in the spanwise direction. In order to trigger vortex synchronization, a sinusoidal streamwise

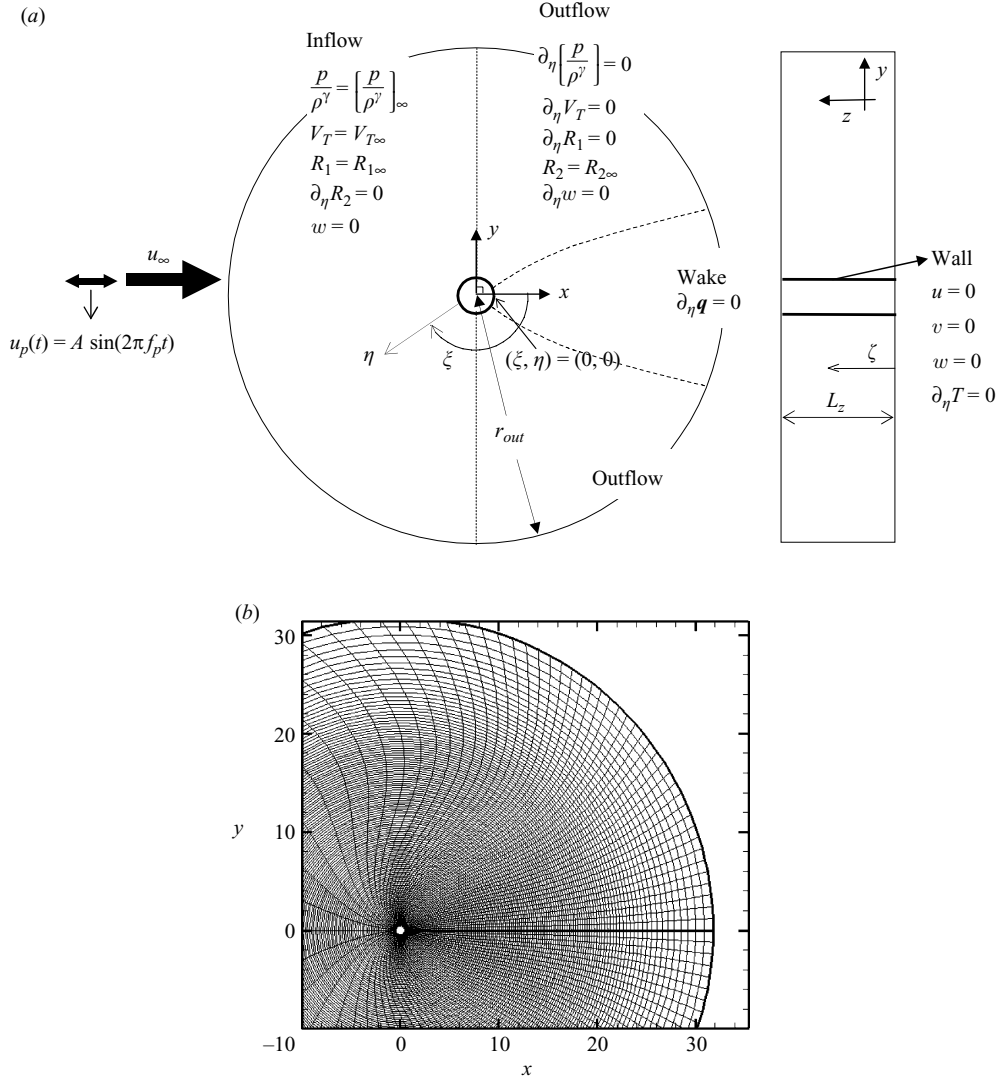


FIGURE 1. (a) Schematics of coordinate system and boundary conditions and (b) O-type grid generation adopted for the present simulations: only the wake region is shown for clarity.

perturbation velocity  $\Delta U$  is superimposed on the uniform inflow velocity  $U_\infty$ , which can be written in non-dimensional form as follows:

$$u_p(t) = A \sin(2\pi f_p t), \quad (2.5)$$

where  $A = \Delta U / U_\infty$  and  $f_p$  is the non-dimensionalized perturbation frequency.

As shown in figure 1(b), the grid is clustered near the cylinder surface and the wake region. Domain radius is chosen to be large enough for the computational results not to be affected by the boundary conditions through intensive parametric studies on the domain size. Chosen domain size is  $r_{out} = 32D$ , which is also consistent with the proposal of Kwon & Choi (1996). Spanwise domain size  $L_z = 3.5\pi D$  is chosen to allow three or four pairs of streamwise vortices for the mode-A instability at  $Re = 220$ ,

whose wavelength is between  $3D$  and  $4D$ . Two grid systems, Grid I and Grid II, are adopted for the simulation of unperturbed and perturbed flows, and one additional grid system Grid II\* is adopted for the grid validation. The number of grid points of the Grid I is  $134 \times 97 \times 65$  in the radial, azimuthal and spanwise directions, and that of the Grid II and Grid II\* are  $201 \times 145 \times 129$  and  $201 \times 145 \times 257$ , respectively. The dimensionless time step size is  $\delta t^+ = \delta t U_\infty / D = 0.0025$  for all cases considered. Thus, since the distance between the cylinder wall and the wall-nearest grid point is  $\delta r = 0.005D$  for all cases,  $\delta r^+ = \delta r / \sqrt{\nu \delta t} = 1.5$  at  $Re = 220$  and  $1.9$  at  $Re = 360$ .

The accuracy and efficiency of the numerical method and computer code were already validated through the applications to various turbulent flows (Jin, Park & Yoo 2001; Park *et al.* 2004). For the present study, however, further validations will be given in the subsequent sections by comparing with existing experimental and DNS data for unperturbed natural shedding state at both Reynolds numbers.

### 3. Results and discussions

First, results for the natural shedding state at each Reynolds number is presented for code validation. Then, conditions required for the occurrence of vortex synchronization are analysed. Finally, discussions are carried out on changes in global parameters, trajectory of the vortex centre, force balance for the mean wake bubble and vortex structure due to the occurrence of vortex synchronization.

#### 3.1. Natural shedding state

Figure 2 shows profiles of the mean velocity ( $\bar{u}$  and  $\bar{v}$ ) and the Reynolds normal stress ( $\overline{u'u'}$  and  $\overline{v'v'}$ ) components in the streamwise and cross-stream directions for the natural shedding state at  $Re = 360$ , where  $\bar{(\cdot)}$  and  $(\cdot)'$  denote the time-averaged mean and its fluctuations, respectively. In order to examine grid sensitivity, we compare these profiles at five locations in the near wake region, which are obtained with Grid I, Grid II and Grid II\*, with other DNS data at  $Re = 300$  obtained by Mittal & Balachandar (1997). Although  $Re$  is slightly different, the present results are all in excellent agreement with those of Mittal & Balachandar. It is also shown that except for  $\overline{v'v'}$  at  $x \geq 5$ , the three solutions obtained with the three grids are nearly identical to each other, implying that the present simulations are not quite sensitive to the grid resolution, probably due to the low-Reynolds-number characteristics. Therefore, we judge that it should be safe to use Grid I as the baseline grid of the present simulations without sacrificing the accuracy significantly. However, we still decide to use Grid II for the present simulation at  $Re = 360$  in order to be more conservative.

In the present study,  $St$  is determined on the basis of the shedding frequency obtained from the average peak-to-peak distance of the oscillating lift coefficient ( $C_L$ ) curve (see figure 10) for 30 cycles after the quasi-steady states. In figure 3, the predicted Strouhal numbers ( $St$ ) for the natural shedding states at  $Re = 220$  and  $360$  are compared with the existing experimental data represented by the  $St$ - $Re$  relationship. As is clearly shown, the present data for  $St = 0.184$  and  $0.201$  at  $Re = 220$  and  $360$ , respectively, agree very well with the experimental data. Some other important parameters such as the mean base suction pressure coefficient  $-\bar{C}_{pb}$ , mean drag coefficient  $\bar{C}_D$  and the root-mean-square lift coefficient  $(C_L)_{rms}$  are also shown to be in good agreement with other DNS or experimental data, as summarized in table 1.

Figure 4 shows the qualitative comparison of the vortical structures visualized from the present DNS and the experiment of Williamson (1996c) for natural shedding

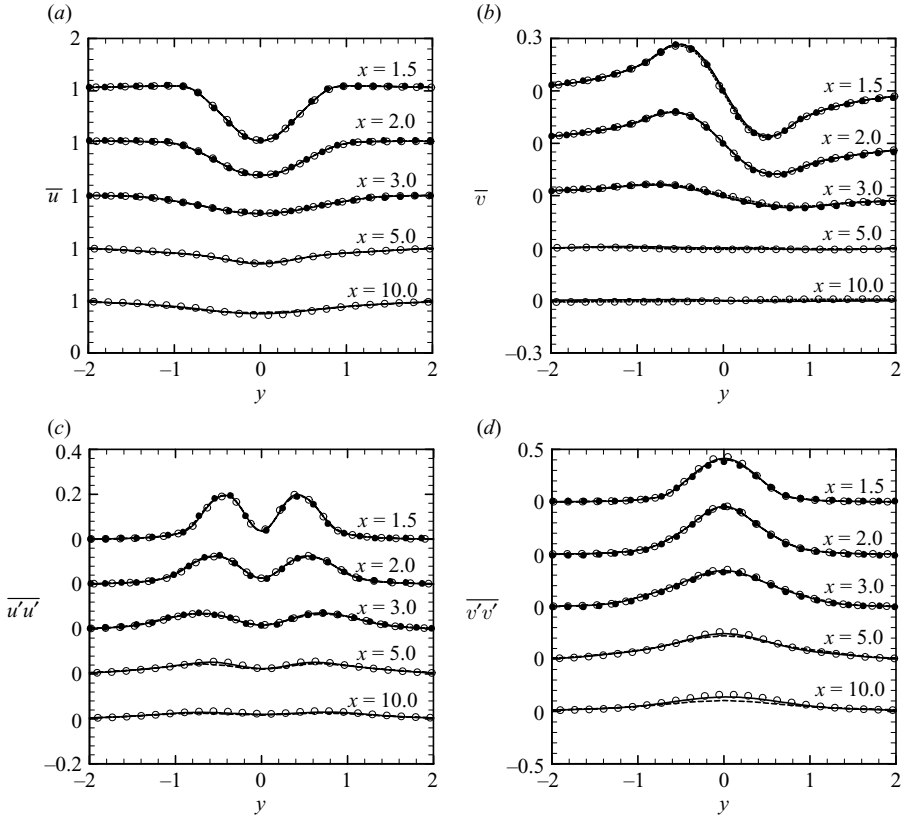


FIGURE 2. Mean velocity and Reynolds normal stress profiles at 5 downstream locations for the natural shedding state at  $Re = 360$ : - - -, Grid I; —, Grid II;  $\circ$ , Grid II\*;  $\bullet$ , Mittal & Balachandar (1997),  $Re = 300$ . (a)  $\bar{u}$ , (b)  $\bar{v}$ , (c)  $\overline{u'u'}$ , (d)  $\overline{v'v'}$ .

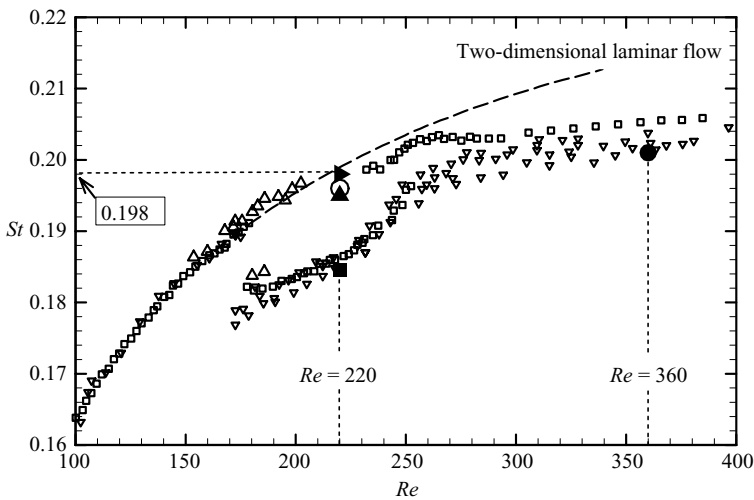


FIGURE 3. Strouhal–Reynolds number relationship for the natural shedding state:  $\square$ , Williamson (1992);  $\nabla$ , Fey, König & Eckelmann (1998);  $\triangle$ , Miller & Williamson (1994); - - -, Posdziech & Grundmann (2001);  $\bullet$ , the present study at  $Re = 360$ ;  $\blacksquare$ , the present study at  $Re = 220$ . The Strouhal numbers obtained by the present study for the perturbed cases at  $Re = 220$  (see table 2) are also indicated for later discussion:  $\circ$ , Case I-2;  $\blacktriangle$ , Case I-3;  $\blacktriangleright$ , Case I-4.

$Re$	Instability Mode	Methodology	$-\bar{C}_{pb}$	$\bar{C}_D$	$(C_L)_{rms}$
220 (present study)	Mode A	DNS	0.89	1.27	0.40
220 <sup>a</sup>	Mode A	DNS	0.91	1.29	0.38
220 <sup>b</sup>	Mode A	Exp.	0.87	—	—
360 (present study)	Mode B	DNS	0.99	1.24	0.39
330 <sup>c</sup>	Mode B	DNS	1.00	1.25	0.43
350 <sup>b</sup>	Mode B	Exp.	0.96	—	—

TABLE 1. Characteristic mean properties for each wake transition mode: <sup>a</sup>Kim & Choi (2005), <sup>b</sup>Williamson & Roshko (1990), <sup>c</sup>Posdziech & Grundmann (2001).

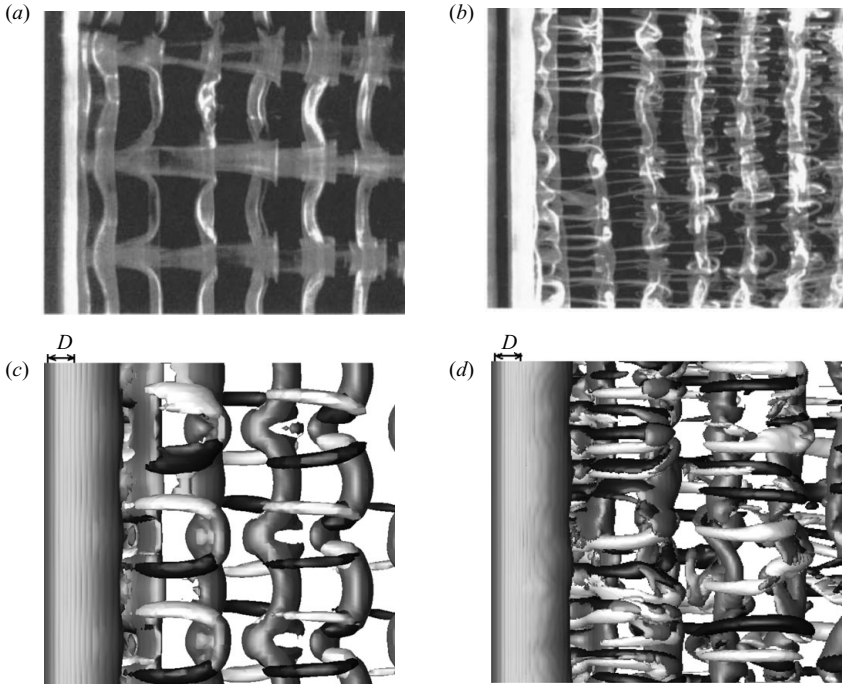


FIGURE 4. Visualization of the vortex structures in the near wake region for two three-dimensional instability modes. (a) Mode-A instability at  $Re=200$  and (b) mode-B instability at  $Re=270$  are experimentally captured by Williamson (1996b). Visualizations of vorticity field for the present study are plotted for (c) mode-A instability at  $Re=220$  and (d) mode-B instability at  $Re=360$ : light grey,  $\omega_x = +0.8$ ; black,  $\omega_x = -0.8$ ; dark grey,  $\omega_z = \pm 0.8$ .

states in mode-A and mode-B wake transition regimes. Figures 4(a) and 4(b) are the experimental visualization obtained at  $Re=200$  (mode A) and 270 (mode B), and figures 4(c) and 4(d) show the present results at  $Re=220$  and 360, respectively. According to Williamson (1996b), mode-A instability begins with a wavy deformation of the primary Kármán vortices, and accordingly the counter-rotating streamwise vortex pair begins to appear in the wake. As shown in figure 4(c), this feature of the streamwise vortex structure is clearly observed in the present DNS at  $Re=220$ . The average spanwise wavelength of these streamwise vortex pairs, measured by peak-to-peak distance of streamwise vorticity contours, is about  $3.6D$  in this case, which



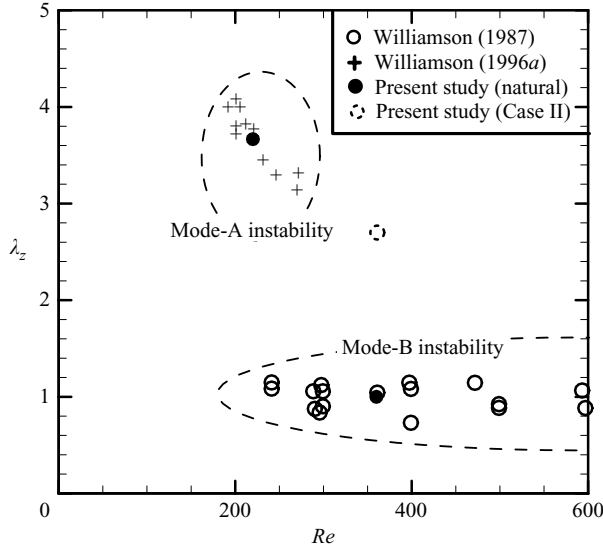


FIGURE 5. Normalized spanwise wavelength ( $\lambda_z$ ) of the streamwise vortex pair as a function of the Reynolds number.  $\lambda_z$  for Case II will be discussed in §3.3.4.

$Re$	Case	$A/(\pi f_p)$	$f_p$	Remarks
220	Case I-1	0.04	0.306	
	Case I-2	0.04	0.336	
	Case I-3	0.04	0.368	$f_p = 2f_n$
	Case I-4 <sup>a</sup>	0.04	0.396	
	Case I-5	0.04	0.426	
360	Case II <sup>a</sup>	0.04	0.402	$f_p = 2f_n$

TABLE 2. Conditions of the sinusoidal perturbation at each Reynolds number. <sup>a</sup>The vortex shedding frequency is related to the perturbation frequency by  $f_s = 0.5f_p$ .

is in very close agreement with other experimental data (see figure 5). For mode-B instability, figure 4(b) shows that the streamwise vortices are more closely packed in the spanwise direction at higher  $Re$  so that its average spanwise wavelength is shortened, i.e. it becomes about  $1D$  according to Williamson (1987, 1996c). As shown in figures 4(d) and 5, this feature is also well captured in the present simulation at  $Re = 360$ , where the predicted streamwise vortical structure as well as its wavelength is in very good agreement compared with the experimental data.

### 3.2. The occurrence of synchronization

Table 2 shows the flow conditions covered in the present study to investigate the vortex synchronization phenomena in perturbed flows. As in the previous studies on vortex lock-on in the case of oscillatory incident flow (Barbi *et al.* 1986; Konstantinidis *et al.* 2003), we use normalized peak-to-peak velocity perturbation amplitude given by the ratio of displacement to cylinder diameter,  $2a/D = 2\Delta U/(\omega D) = 2AU_\infty/(\omega D)$ , where  $\omega$  is normalized by  $U_\infty/D$  such that  $\omega D/U_\infty = 2\pi f_p$ . For all cases, this normalized

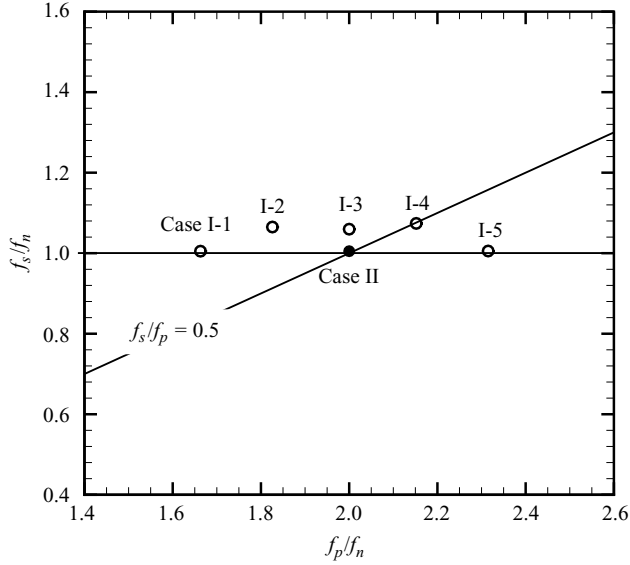


FIGURE 6. Variation of vortex shedding frequency with perturbation frequency:  $\circ$ , Case I-1, Case I-2, Case I-3, Case I-4 and Case I-5 at  $Re = 220$ ;  $\bullet$ , Case II at  $Re = 360$ . When vortex synchronization occurs,  $f_s$  is related to  $f_p$  by  $f_s/f_p = 0.5$ , so that only Case I-4 and Case II correspond to vortex synchronization.

velocity perturbation amplitude is held constant at  $2A/(2\pi f_p) = 0.04$  in order to avoid additional complexities due to amplitude variations. The non-dimensionalized perturbation frequency ( $f_p$ ) is used as the parameter to find the synchronization condition at each Reynolds number. At  $Re = 220$ , referred to as Case I, we consider five subcases in the range of frequencies,  $0.306 \leq f_p \leq 0.426$ , such that Case I-1 and Case I-5 correspond to the lower and upper bounds of the range, i.e.  $f_p = 0.306$  and  $0.426$ , respectively; Case I-2 corresponds to the middle of the frequencies for Case I-1 and Case I-3, i.e.  $f_p = 0.336$ ; Case I-3 corresponds to exactly twice the natural shedding frequency ( $f_n = 0.184$ ), i.e.  $f_p = 0.368$ ; Case I-4 corresponds to twice the shedding frequency ( $St = 0.198$ ) near the two-dimensional laminar flow regime (see figure 3), i.e.  $f_p = 0.396$ . Unlike these five conditions at  $Re = 220$ , only one perturbation condition is considered at  $Re = 360$ . This is because Kim *et al.* (2006) already showed that the vortex synchronization occurs at  $f_p = 2f_n$  at this Reynolds number so that there is no need to cover a range of frequencies to search for the synchronization condition. Since the present study can be considered as a follow-on study of their work, by using DNS, we will consider here exactly the same condition as considered by them, i.e.  $f_p (= 2f_n) = 0.402$ , which is designated as Case II in the present study (see table 2).

In order to check the occurrence of vortex synchronization in each case, we consider the relation between  $f_s$  and  $f_p$  after normalizing them with  $f_n$  at each  $Re$ , as shown in figure 6, where  $f_s$  is obtained from the average peak-to-peak distance of the oscillating  $C_L$  curve for 30 cycles after the quasi-steady states. This is because in a previous experimental study on vortex shedding and synchronization behind a circular cylinder in oscillatory flow, Barbi *et al.* (1986) showed that  $f_s$  is related to  $f_p$  by  $f_s/f_p = 0.5$  when the vortex synchronization occurs in a perturbed flow. As

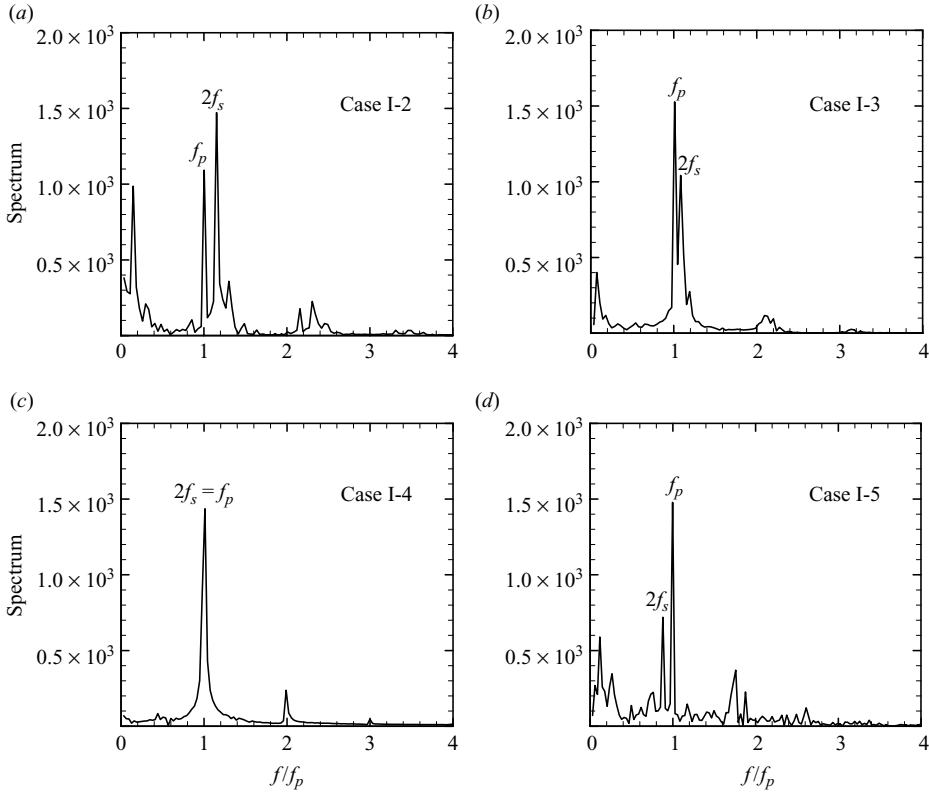


FIGURE 7. Spectra corresponding to streamwise velocity signal obtained at  $x=5$  along the wake centreline in (a) Case I-2, (b) Case I-3, (c) Case I-4 and (d) Case I-5 ( $Re=220$ ).

expected, the vortex synchronization in Case II at  $Re=360$  is observed to occur when the measured  $f_s$  exactly matches half the imposed  $f_p$ , as shown in figure 6. This result is consistent with the previous experimental study of Kim *et al.* (2006) using PIV. Quite interestingly, however, Case I-3 at  $Re=220$  does not show a clear indication of the vortex synchronization although the imposed perturbation condition is the same as that in Case II, i.e.  $f_p=2f_n$ . Instead, it is shown that at this Reynolds number the vortex synchronization actually occurs at  $f_p=0.396$  (Case I-4 in figure 6) since the predicted  $f_s$  exactly matches with the Barbi's synchronization relationship of  $f_s/f_p=0.5$ .

The occurrence of vortex synchronization in Case I-4 can be also seen from the discrete Fourier transform (DFT) results of the streamwise velocity signal obtained at  $x=5$  along the wake centreline. Figure 7 shows these DFT results in Case I-2, Case I-3, Case I-4 and Case I-5, in which the abscissa is normalized by  $f_p$ . In each case, there always exists a peak at  $f/f_p=1$ , but in Case I-2, Case I-3 and Case I-5, another dominant peak is also shown to occur near  $f/f_p=1$ , which corresponds to twice the shedding frequency ( $f_s$ ) in each case. Quite unlike these other cases, only Case I-4 shows a single dominant peak at  $f/f_p=1$ , implying that at this condition the vortex shedding occurs exactly at a frequency of  $f_s=0.5f_p$ . These DFT results clearly indicate that the vortex synchronization occurs only in Case I-4 among various cases considered in the present study at  $Re=220$ .

The reason that vortex synchronization occurs in Case I-4 can be explained through the examination of  $f_s$ . The predicted  $f_s$  in both Case I-1 and Case I-5 is 0.185 which is approximately the same as  $f_n = 0.184$ . On the other hand, in Case I-2, Case I-3 and Case I-4,  $f_s$  is modified from  $f_n$ . That is, the predicted  $f_s$  increases to 0.196, 0.195 and 0.198, respectively. Very interestingly, these increased  $f_s$ s in the three cases are shown to exist near the value corresponding to two-dimensional laminar vortex shedding frequency (see figure 3), implying that the wake transition is suppressed in these three cases. From these results, we can conclude that at  $Re = 220$ , vortex synchronization occurs when the perturbation frequency is not near twice the natural shedding frequency but near twice the modified shedding frequency due to the suppression of wake transition. Thus, vortex synchronization occurs in Case I-4 where  $f_p$  is twice the value corresponding to suppressed wake transition regime. The verification of the suppression of wake transition will be discussed in more detail in the following subsection.

### 3.2.1. Suppression of wake transition

If the wake transition is suppressed, the three-dimensionality of the flow will be significantly diminished. This can be shown by using two flow quantities introduced by Poncet (2002): the spanwise enstrophy

$$Z_z = \int_{\Omega} \omega_z^2 dV, \quad (3.1)$$

and orthogonal enstrophy

$$Z^{\perp} = \int_{\Omega} (\omega_x^2 + \omega_y^2) dV, \quad (3.2)$$

where  $\Omega$  represents the whole computational domain, and  $\omega_x$ ,  $\omega_y$  and  $\omega_z$  denote the streamwise, cross-stream and spanwise vorticity components, respectively. Figure 8(a) shows time history of  $Z^{\perp}$  in each case at  $Re = 220$ . As shown in this figure, the predicted  $Z^{\perp}$  in Case I-1 and Case I-5 does not vanish with time, which means that there remains a significant three-dimensionality in the flow. In Case I-2, Case I-3 and Case I-4, on the other hand,  $Z^{\perp}$  is shown to decrease with time and it eventually vanishes, indicating that there exists little three-dimensionality in the flow in these cases. Figure 8(b) shows time histories of  $Z_z$  only in Case I-3, Case I-4 and Case I-5, since the time histories of  $Z_z$  show similar tendencies, respectively, in Case I-1 and Case I-5, and in Case I-2 and Case I-3. It is shown that the mean values of  $Z_z$  in Case I-3 and Case I-4 are higher than that in Case I-5, implying that the Kármán vortex becomes stronger. From the observations of modification of the Strouhal number and vanishing three-dimensionality of the flow, we can conclude that the wake transition behind the circular cylinder is suppressed in Case I-2, Case I-3 and Case I-4 (Yoo, Kim & Bae 2006).

### 3.2.2. Vortex synchronization regime

Suppression of wake transition affects the shape of vortex synchronization regime which is defined on the basis of the perturbation amplitude and frequency. Figure 9(a) shows the limit of general vortex synchronization regime at various Reynolds numbers (Konstantinidis *et al.* 2003). As shown in the figure, the trough of the vortex synchronization regime is formed around the point corresponding to twice  $f_n$ . In the meanwhile, figure 9(b) shows the vortex synchronization regime at  $Re = 190$  obtained

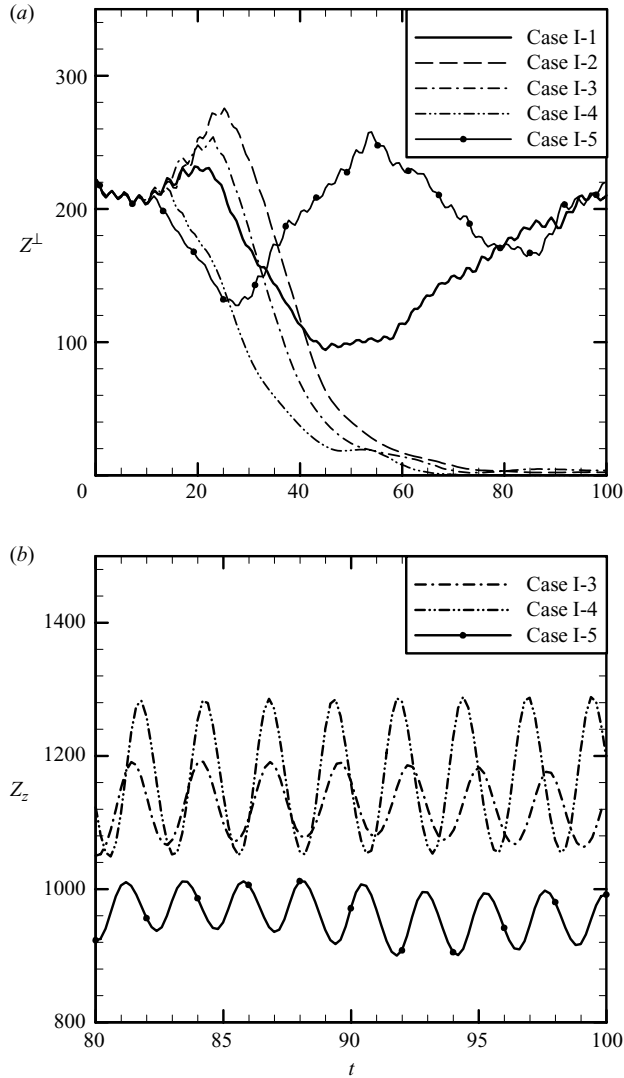


FIGURE 8. Time histories of (a)  $Z^\perp$  and (b)  $Z_z$  at  $Re = 220$ , where  $Z^\perp$  and  $Z_z$  are defined as  $\int_{\Omega} (\omega_x^2 + \omega_y^2) dV$  and  $\int_{\Omega} \omega_z^2 dV$ , respectively.

by Griffin & Ramberg (1976) and the perturbation conditions for the present study at  $Re = 220$ . The trough of the vortex synchronization regime of Griffin & Ramberg (1976) seems to be shifted towards the point corresponding to more than twice  $f_n$ . Quite interestingly, the point corresponding to Case I-4 seems to be the trough of this vortex synchronization regime although  $Re$  is slightly different. It indicates that the trough of the vortex synchronization regime in mode-A regime is formed, depending not on  $f_n$  but on the modified shedding frequency due to the suppression of the wake transition (Yoo *et al.* 2006).

### 3.3. Changes due to the occurrence of the vortex synchronization

Occurrence of vortex synchronization causes several changes in the wake behind the circular cylinder. In order to investigate these changes and compare them between

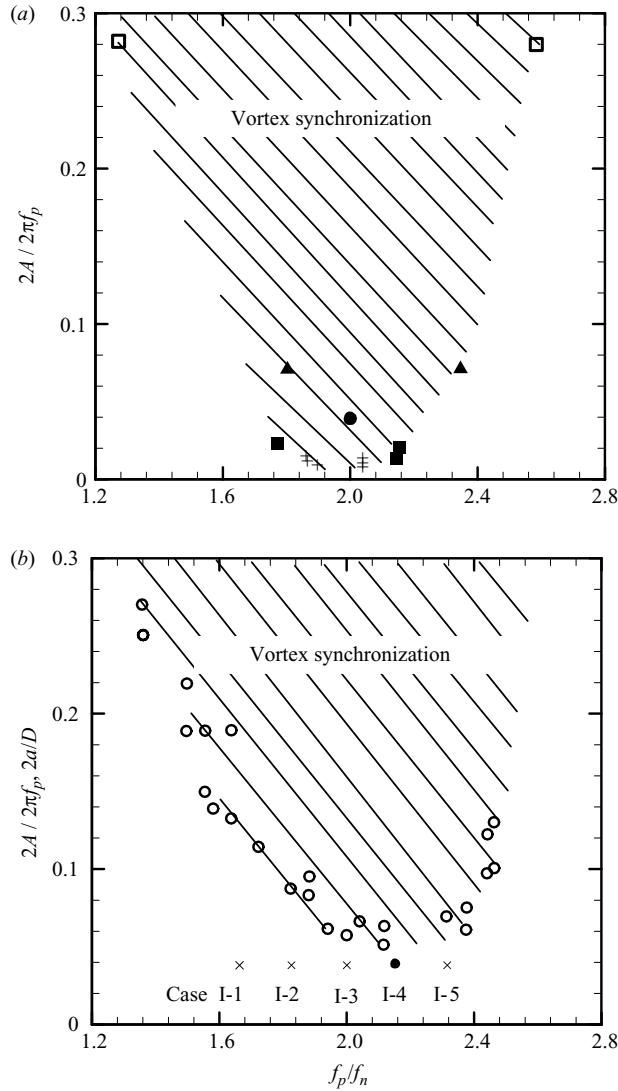


FIGURE 9. Limits of the vortex synchronization regime as functions of perturbation amplitude and frequency. (a) General vortex synchronization regime: □, Tanida, Okajima & Watanabe (1973) at  $Re = 4000$ ; ■, Konstantinidis *et al.* (2003) at  $Re = 21500$ ; +, Armstrong, Barnes & Grant (1986) at  $Re = 21500$ ; ▲, Barbi *et al.* (1986) at  $Re = 3000$ ; ●, present study with synchronization at  $Re = 360$ . (b) Vortex synchronization regime for mode-A instability regime: ○, Griffin & Ramberg (1976) at  $Re = 190$ ; ●, present study with synchronization at  $Re = 220$ ; ×, present study without synchronization at  $Re = 220$ .

$Re = 220$  and  $360$ , we will discuss global parameters, trajectories of the vortex centre, force balance of the mean wake bubble and vortex structures.

### 3.3.1. Global parameters

Table 3 shows the global parameters at each  $Re$ , where the length of the mean wake bubble  $x_L$  is measured from the centre of the cylinder to the location of zero mean velocity (reattachment point). For comparison, the values of  $x_L$  obtained by Kim *et al.* (2006) using PIV are also included. Due to the vortex synchronization,

$Re$	State	$x_L$	$-\bar{C}_{pb}$	$\bar{C}_D$	$(C_D)_{rms}$	$u_e$
220 (present study)	Natural	1.54	0.89	1.28	0.02	1.31
	Synchronization	1.10	1.09	1.43	0.52	1.33
360 (present study)	Natural	1.44	0.99	1.24	0.04	1.34
	Synchronization	0.98	1.29	1.42	0.41	1.36
360 (Kim <i>et al.</i> 2006)	Natural	1.67	—	—	—	1.27
	Synchronization	1.06	—	—	—	1.35

TABLE 3. Comparison of global parameters between the natural shedding and synchronization states at each Reynolds number.

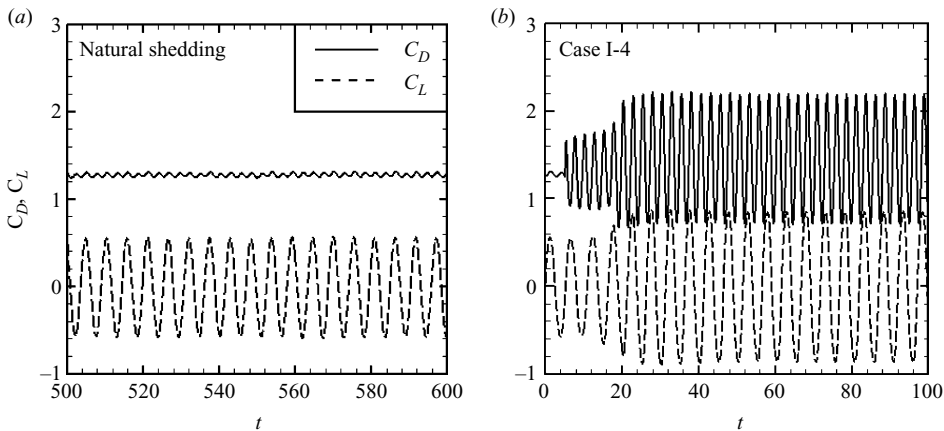


FIGURE 10. Time histories of  $C_D$  and  $C_L$  for the natural shedding state at  $Re = 220$  and for the vortex synchronization state in Case I-4 where the flow was perturbed for  $t \geq 0$ .

the predicted  $x_L$  is shortened from 1.54 to 1.10 at  $Re = 220$  and from 1.44 to 0.98 at  $Re = 360$ , respectively. There exist some discrepancies in the magnitude of  $x_L$  between DNS and PIV data, which seems to be due to the low aspect ratio of circular cylinder used for PIV experiment of Kim *et al.* (2006). However, variation of  $x_L$  due to the occurrence of vortex synchronization is shown to be in reasonable agreement between DNS and PIV data. That is,  $x_L$  is shortened with vortex synchronization about 32% and 36% for DNS and PIV, respectively. Other important parameter  $-\bar{C}_{pb}$  is increased by about 22% and 30% at  $Re = 220$  and 360, respectively, which is related to the increase of the drag force. Figure 10 illustrates the  $C_D$  and  $C_L$  for the natural shedding state at  $Re = 220$  and for the vortex synchronization state at  $Re = 220$  (i.e. Case I-4). Perturbation is introduced for  $t \geq 0$  in Case I-4, and after about 30 time units, the flow reaches a time-periodic state. A remarkable change is observed for  $C_D$  curves. As shown in table 3,  $(C_D)_{rms}$  significantly increases from 0.02 to 0.52 at  $Re = 220$  and from 0.04 to 0.41 at  $Re = 360$  due to the vortex synchronization. The mean values of drag coefficient  $\bar{C}_D$  also increases from 1.28 to 1.43 at  $Re = 220$  and from 1.24 to 1.42 at  $Re = 360$ , respectively.

### 3.3.2. Trajectory of the vortex centre

We investigate the motion of the Kármán vortices by observing the trajectories of the vortex centre which are determined by the same method as used in Kim *et al.* (2006). Figure 11 shows the trajectories of the vortex centre, superimposed on  $\overline{u'v'}$

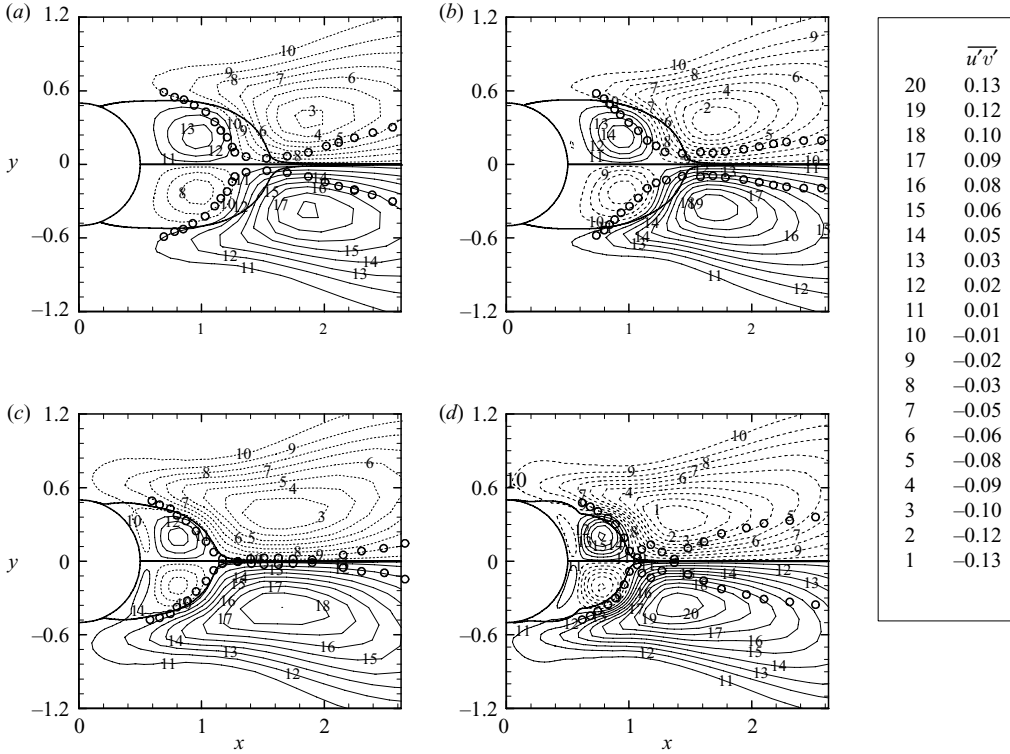


FIGURE 11. Comparison of the trajectories of the vortex centre, superimposed on  $\overline{u'v'}$  distributions for the natural shedding states at (a)  $Re = 220$  and (b)  $Re = 360$ , and for the vortex synchronization states in (c) Case I-4 and (d) Case II. Solid lines denote mean separating streamlines and open circles denote the loci of vortex centres.

distributions, where open circles denote the loci of vortex centres traced at time intervals of 0.25 and solid lines denote the mean separating streamlines. Figures 11(a) and 11(b) show trajectories of the vortex centre for the natural shedding states at  $Re = 220$  and 360, and figures 11(c) and 11(d) show them in Case I-4 and Case II, respectively. For the natural shedding state at each Reynolds number, the Kármán vortices are gradually formed inside the mean wake bubble and move downstream as shown in figures 11(a) and 11(b). Occurrence of vortex synchronization, on the other hand, changes these trajectories of vortex centre. In both Case I-4 and Case II, the Kármán vortices are formed along the mean separating streamline and the paths of vortices shed in the upper and lower parts meet together at the reattachment point, as shown in figures 11(c) and 11(d). It is particularly interesting to note that the present results at  $Re = 360$  are consistent with those of Kim *et al.* (2006). Behind the reattachment point, the Kármán vortices move downstream, fluctuating along the wake centreline in Case I-4 and more dynamically in Case II. Interestingly, we find a slight difference in trajectories of vortex centre around the mean wake bubble between Case I-4 and Case II. That is, the Kármán vortices are formed near the mean separating streamline slightly inside the mean wake bubble in Case I-4 while slightly outside in Case II. We pay attention to this difference because the trajectory of the Kármán vortices around the mean wake bubble affects the force balance of the mean wake bubble, which will be discussed in the following subsection.



### 3.3.3. Force balance of the mean wake bubble

Balachandar *et al.* (1997) and Kim *et al.* (2006) analysed the force balance of the mean wake bubble in the time-averaged and two-dimensional sense to investigate the interaction between the shear layers resulting in the Kármán vortex shedding. The non-dimensionalized streamwise force balance inside the mean wake bubble for the compressible flow can be written as

$$\int_{\partial\Omega} \bar{p} n_x ds + \int_{\partial\Omega} \left\{ \overline{\rho u' u'} - \frac{\bar{\mu}}{Re} \left( \frac{4\partial\bar{u}}{3\partial x} - \frac{2\partial\bar{v}}{3\partial y} \right) \right\} n_x ds \\ = - \int_{\partial\Omega} \left\{ \overline{\rho u' v'} - \frac{\bar{\mu}}{Re} \left( \frac{\partial\bar{u}}{\partial y} + \frac{\partial\bar{v}}{\partial x} \right) \right\} n_y ds, \quad (3.3)$$

where  $\partial\Omega$  represents the boundary of the mean wake bubble,  $n_x$  and  $n_y$  are the direction cosines of the outward unit normal vector on the boundary of the mean wake bubble. The triple fluctuation components and density fluctuations are neglected on the ground of the low Mach number of  $M=0.2$  (Morkovin's hypothesis). For simplicity and direct comparison with PIV data of Kim *et al.* (2006), three terms in (3.3) such as  $\int_{\partial\Omega} (4\bar{\mu}\partial\bar{u}/3Re\partial x)n_x ds$ ,  $\int_{\partial\Omega} (2\bar{\mu}\partial\bar{v}/3Re\partial y)n_x ds$  and  $\int_{\partial\Omega} (\bar{\mu}\partial\bar{v}/Re\partial x)n_y ds$  are neglected (in fact, each of these terms is less than 5% of the dominant term in each case). After this approximation, (3.3) takes the form

$$\int_{\partial\Omega} C_p n_x ds + \int_{\partial\Omega} C_n n_x ds \approx \int_{\partial\Omega} C_\tau n_y ds + \int_{\partial\Omega} C_{\tau v} n_y ds. \quad (3.4)$$

Each coefficient is defined as follows:

$$C_p = \frac{\bar{p} - \bar{p}_b}{\frac{1}{2}\bar{\rho}u_e^2}, \quad C_n = \frac{\overline{\rho u' u'}}{\frac{1}{2}\bar{\rho}u_e^2}, \quad C_\tau = -\frac{\overline{\rho u' v'}}{\frac{1}{2}\bar{\rho}u_e^2}, \quad C_{\tau v} = \frac{\frac{\bar{\mu}}{Re} \frac{\partial\bar{u}}{\partial y}}{\frac{1}{2}\bar{\rho}u_e^2}, \quad (3.5)$$

where  $\bar{p}_b$  is the non-dimensionalized mean pressure at the base of the cylinder and  $u_e$  is the velocity at the edge of the separated shear layer, which is non-dimensionalized by  $U_\infty$  (see table 3 for values of  $u_e$ ). The terms on the left-hand side of (3.4) account for the net  $x$  direction force due to the pressure and the Reynolds normal stress. Two terms on the right-hand side account for the net  $x$  direction forces due to the Reynolds shear and viscous shear stresses. From now onwards, each term of (3.4) will be represented as  $[C_p]$ ,  $[C_n]$ ,  $[C_\tau]$  and  $[C_{\tau v}]$  for convenience sake.

Figure 12 shows the distributions of  $C_n$  and  $C_\tau$  for the natural shedding state and the vortex synchronization state (Case II) at  $Re=360$  along the path of separation point ( $S$ ), reattachment point ( $R$ ) and base point ( $B$ ), i.e. the boundary of the top half of the mean recirculation region, where the integrated areas inside the closed curves represent the net forces acting on the mean wake bubble by the Reynolds normal and shear stresses. Left figures show the natural shedding states and right figures show the vortex synchronization states, where PIV data of Kim *et al.* (2006) are also included for comparison. The distributions of DNS and PIV data show general agreement with each other except  $C_\tau$  distribution near reattachment points due to different definition of  $x_L$ . In particular, as a result of the vortex synchronization, the changes in the distributions of  $C_n$  and  $C_\tau$  indicated by both DNS and PIV data showed consistent tendencies (Yoo, Park & Park 2005). That is, the magnitude of  $C_n$  is reduced as noticed by comparing figures 12(a) and 12(b), and the sign of  $C_\tau$  is changed along the path of  $S-R$ , as noticed by comparing figures 12(c) and 12(d). In figure 13, we plotted

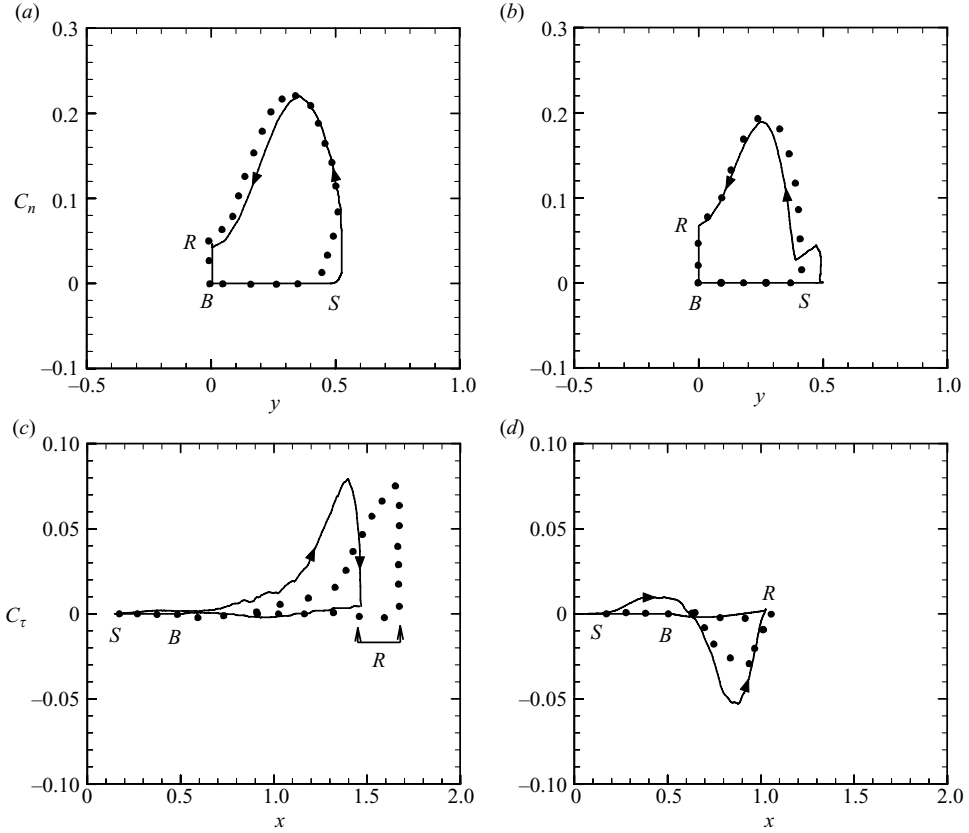


FIGURE 12. Distributions of  $C_n$  and  $C_\tau$  along the path of separation point (S), reattachment point (R) and base point (B) at  $Re = 360$ . Figures (a) and (c) show the natural shedding state, and (b) and (d) show the vortex synchronization state (Case II). Figures (a) and (b) show distributions of  $C_n$ , and figures (c) and (d) show distributions of  $C_\tau$ : —, DNS (present data); ●, PIV (Kim *et al.* 2006).

$C_\tau$  distributions for the natural shedding state and the vortex synchronization state at  $Re = 220$  (Case I-4), to compare the change in the distributions of  $C_\tau$  with that at  $Re = 360$ . Since the magnitude of  $C_n$  is also reduced due to the vortex synchronization in Case I-4 (not shown for brevity), similar to Case II, only the distributions of  $C_\tau$  are compared. It is noticeable that unlike in Case II, Case I-4 shows that the sign of  $C_\tau$  is not reversed but its magnitude is significantly diminished along the path of S–R. This difference in the distribution of  $C_\tau$  can be explained through the relationship between the mean separating streamline and the trajectory of the Kármán vortices around the mean wake bubble. According to Kim *et al.* (2006), when the trajectories of the Kármán vortices are formed inside the mean wake bubble, outside the mean wake bubble and on the mean separating streamline, the sign of  $C_\tau$  will be positive (coincident with the streamwise direction), and negative, and the magnitude of  $C_\tau$  will be negligible along the path of S–R, respectively (see figure 18 of Kim *et al.* 2006). In the present study, the Kármán vortices in Case I-4 are formed near the mean separating streamline slightly inside the mean wake bubble while in Case II they are formed slightly outside the mean wake bubble as mentioned above (see figures 11c

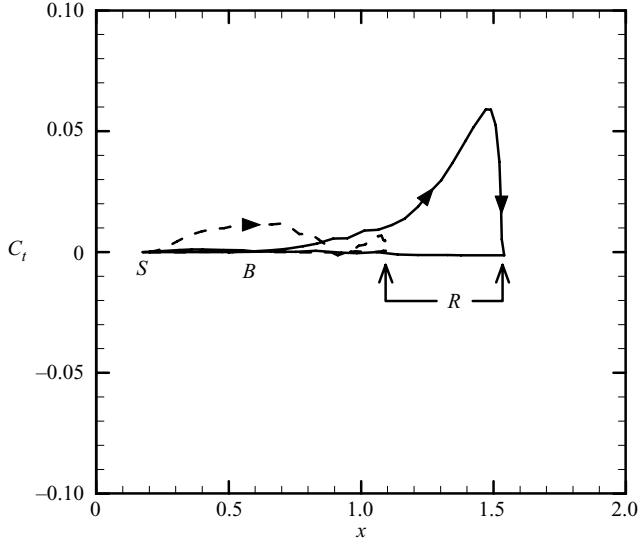


FIGURE 13. Distributions of  $C_\tau$  at  $Re=220$  along the path of separation point ( $S$ ), reattachment point ( $R$ ) and base point ( $B$ ): —, natural shedding state; ---, synchronization state.

$Re$	Case	$[C_p]$	$[C_n]$	$[C_\tau]$	$[C_{\tau v}]$	Remarks
220	Natural	-0.025	0.067	0.017	0.020	Case I-4
	Synchronization	-0.024	0.043	0.005	0.010	
	$\Delta[\cdot]$	-0.001	0.024	0.012	0.010	
360	Natural	-0.038	0.072	0.018	0.014	Case II
	Synchronization	-0.050	0.051	-0.007	0.005	
	$\Delta[\cdot]$	0.012	0.021	0.025	0.009	

TABLE 4. Contributions of respective net force terms to streamwise force balance, which are due to the pressure  $[C_p]$ , Reynolds normal  $[C_n]$  and Reynolds shear  $[C_\tau]$  stresses and viscous shear stress  $[C_{\tau v}]$ , where  $\Delta[\cdot] = [\cdot]_{\text{natural shedding}} - [\cdot]_{\text{synchronization}}$ .

and 11d). For these reasons, the magnitude of  $C_\tau$  is significantly decreased in Case I-4 and its sign is reversed in Case II along the path of  $S$ - $R$ , respectively.

Table 4 summarizes the contributions of respective force terms of (3.4) for natural shedding and vortex synchronization states at each  $Re$ . Note that, for all cases,  $[C_p] + [C_n]$  are well balanced with  $[C_\tau] + [C_{\tau v}]$ , which implies that the approximation of using these four terms is reasonable for considering the force balance of the mean wake bubble at relatively low Reynolds numbers. According to Balachandar *et al.* (1997), among all force terms, contribution of  $[C_n]$  is dominant in the cylinder geometry. As shown in table 4, the present study also shows a consistent result, where contributions of  $[C_n]$  are dominant for natural shedding state at each  $Re$ . The contributions of respective terms, however, are changed differently, depending on the  $Re$  due to the vortex synchronization. The magnitude of  $[C_p]$  is hardly changed in Case I-4 but increased about 30% in Case II, since  $[C_\tau]$  is significantly changed due to reversed direction in Case II, where  $\Delta[C_n]$  and  $\Delta[C_{\tau v}]$  at  $Re = 220$  are comparable with those

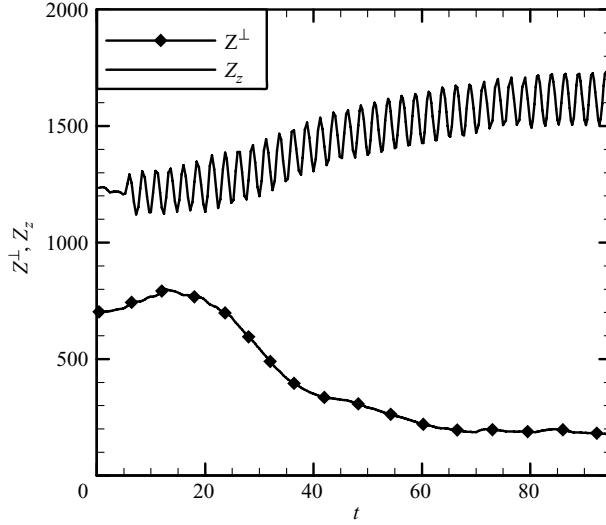


FIGURE 14. Time histories of  $Z^\perp$  and  $Z_z$  in Case II ( $Re = 360$ ).

at  $Re = 360$ . Therefore, the contribution of  $[C_n]$  is still dominant in Case I-4 while the contribution of  $[C_n]$  is comparable with that of  $[C_p]$  in Case II.

### 3.3.4. Vortex structure

As a result of vortex synchronization, vortex structure in the wake behind the circular cylinder is also changed at both  $Re = 220$  and  $Re = 360$ . The growth and decay of spanwise and streamwise vortices are evaluated in terms of the time histories of  $Z_z$  and  $Z^\perp$  in Case II, as shown in figure 14 (time histories in Case I-4 are already shown in figure 8). The mean values of  $Z_z$  and  $Z^\perp$  are gradually increased and decreased, respectively, implying that the Kármán vortex is strengthened while the streamwise vortex is weakened due to the vortex synchronization (Yoo *et al.* 2005). This is similar to what was observed by Poncet (2002, 2004) who triggered vortex synchronization by using rotationally oscillating cylinder at  $Re = 500$  and at  $Re = 400$ , respectively. These changes are visually examined in figure 15. Figures 15(a) and 15(b) show visualized vortex structures for the natural shedding states at  $Re = 220$  and 360, while figures 15(c) and 15(d) show those for the vortex synchronization states in Case I-4 and Case II, respectively, where figures 15(a) and 15(b) are repeatedly included here for better comparison although they are already shown as figures 4(c) and 4(d). In Case I-4, we cannot see any streamwise vortex pair and wavy deformation of the Kármán vortex since the flow behind the circular cylinder has changed into two-dimensional laminar flow, i.e. the three-dimensionality of the flow is vanished (see figure 8a). On the other hand, in Case II, there exist streamwise vortex pairs although their strength is significantly diminished. Moreover, their characteristics are shown to be changed from those of the natural shedding state at  $Re = 360$ , which will be discussed in more detail as follows.

To study qualitatively the characteristics of the streamwise vortex pairs, figures 16, 17 and 18 show  $\omega_x$  contours in the  $y-z$  plane at  $x = 3$  for the natural shedding states at  $Re = 220$  and 360, and for the vortex synchronization state at  $Re = 360$  (Case II), respectively. All the figures 16, 17 and 18 are plotted with the data obtained after reaching quasi-steady states. Especially, figures 18(a) and 18(b) for Case II are plotted with the data obtained at  $t = 87.5$  and  $t = 90.0$ , respectively.  $\omega_x$  contours in

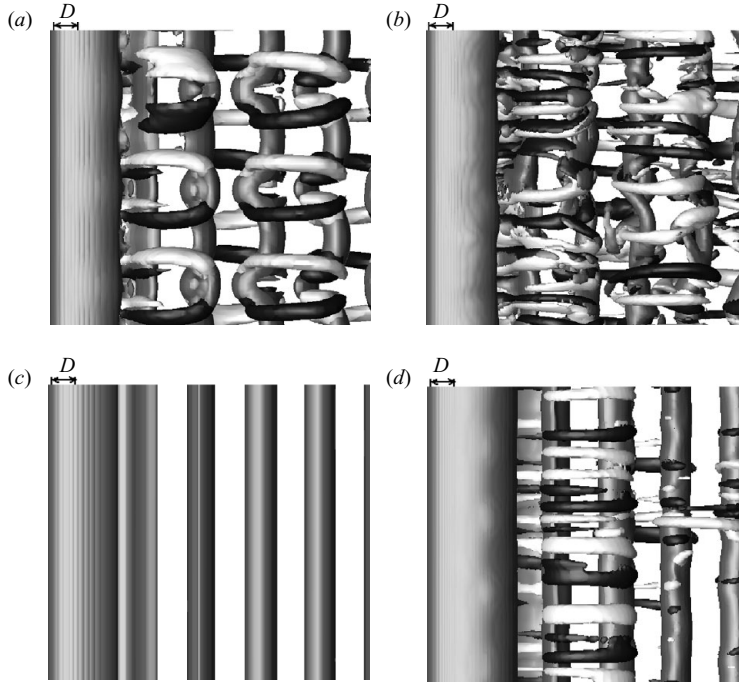


FIGURE 15. Visualization of vorticity field for the natural shedding state at (a)  $Re = 220$  and (b)  $Re = 360$ , and for the vortex synchronization state in (c) Case I-4 and (d) Case II: light grey,  $\omega_x/|\omega_x|_{max} = +0.1$ ; black,  $\omega_x/|\omega_x|_{max} = -0.1$ ; dark grey,  $\omega_z/|\omega_z|_{max} = \pm 0.1$ , where  $|\omega_x|_{max}$  and  $|\omega_z|_{max}$  are maximum values of  $\omega_x$  and  $\omega_z$  in the near wake, respectively. For (a), (b), (c) and (d), the values of  $|\omega_x|_{max}$  are, respectively, 5, 8, 0 and 2, and those of  $|\omega_z|_{max}$  are, respectively, 8, 10, 8 and 14.

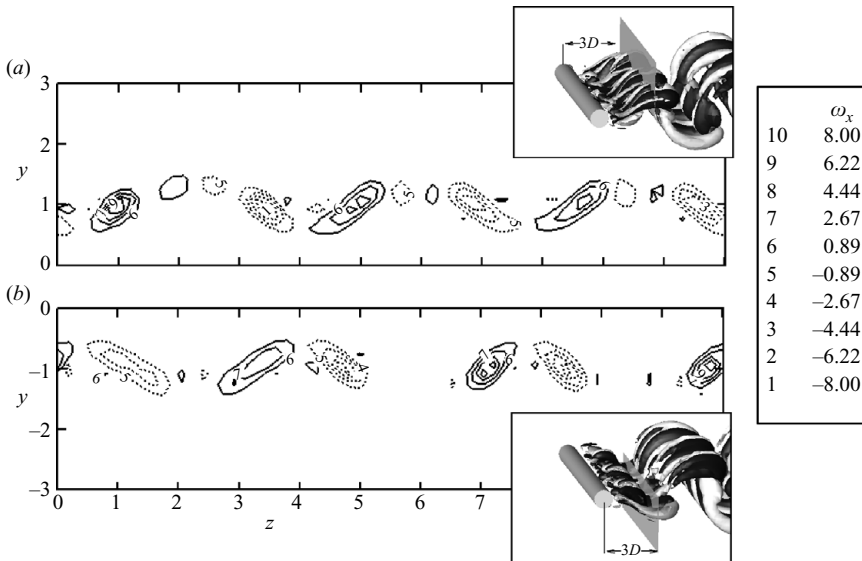


FIGURE 16.  $\omega_x$  contours in the  $y-z$  plane obtained at  $x=3$  for the natural shedding state at  $Re = 220$  (mode-A instability): there is a time lag of half a shedding cycle between (a) and (b).

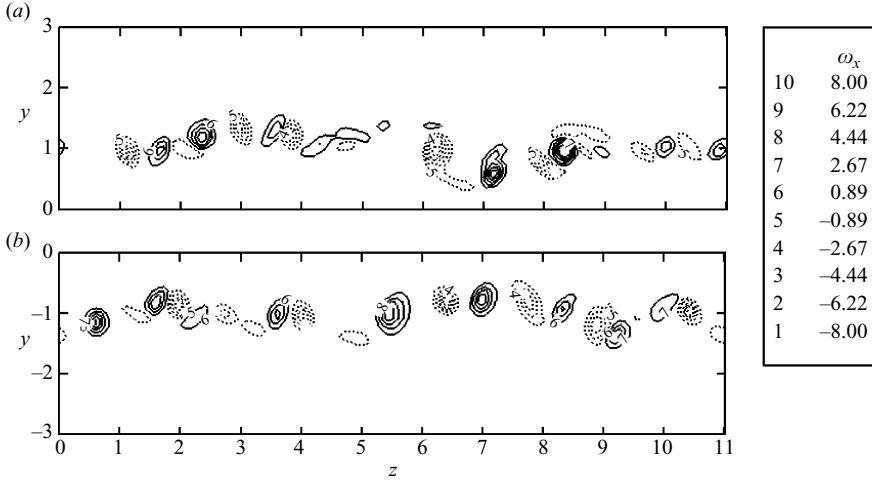


FIGURE 17. Same as figure 16, but for the natural shedding state at  $Re = 360$  (mode-B instability).

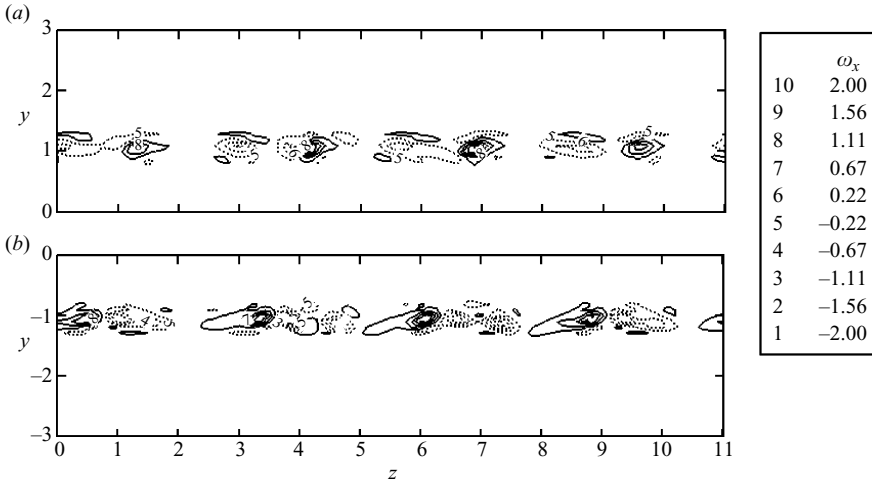


FIGURE 18. Same as figure 16, but for the vortex synchronization state at  $Re = 360$ .

figure 16(a) are plotted at phase = 0 (where the  $C_L$  curve reaches a peak point) while those in figure 16(b) are plotted at phase =  $\pi$ . Hence, figures 16(a) and 16(b) show  $\omega_x$  contours at the same downstream location with opposite  $y$  coordinates at two different moments, where there is a time lag of half a shedding cycle. Figures 17 and 18 are plotted with the same procedure as that of figure 16. According to Williamson (1996b), mode-A instability shows an out-of-phase symmetry due to its physical origin, i.e. wavy deformation of the Kármán vortices. On the other hand, mode-B instability shows an in-phase symmetry pattern since pre-existing streamwise vortices are ‘imprinted’ onto a newly forming braid shear layer (Williamson 1996b). As shown in figures 16 and 17, dominant  $\omega_x$  contours exhibit an out-of-phase symmetry and an in-phase symmetry for the natural shedding state, respectively, at  $Re = 220$  and  $Re = 360$ : the sign of  $\omega_x$  contour is changed at  $Re = 220$  while it is not at  $Re = 360$

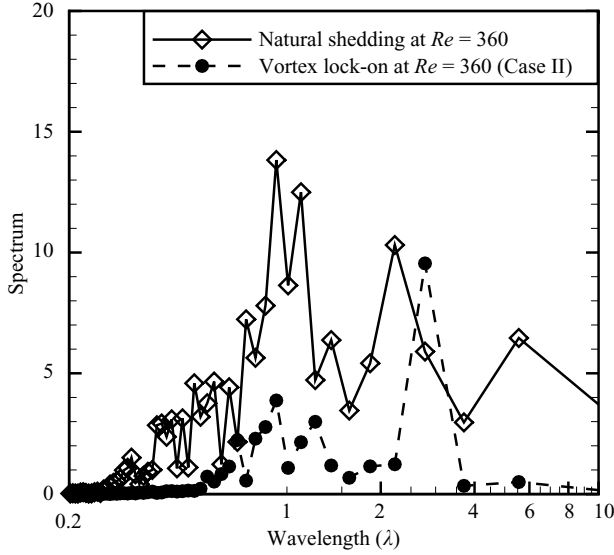


FIGURE 19. Spectra corresponding to  $\omega_x$  obtained along the  $z$ -axis at  $(x, y) = (3, 1)$  for the natural shedding and vortex synchronization (Case II) states at  $Re = 360$ , where abscissa shows wavelength ( $\lambda$ ).

after half a shedding cycle at the same  $z$  position. Interesting features, on the other hand, are observed in Case II as shown in figure 18. That is, unlike the natural shedding state at the same  $Re = 360$ , dominant  $\omega_x$  contours show an out-of-phase symmetry with significantly diminished magnitude (note that the contour level is different).

Moreover, dominant spanwise wavelength of  $\omega_x$  contours in Case II is shown to increase, compared to that for the natural shedding state at  $Re = 360$ . In order to investigate qualitatively this increased wavelength, we performed DFT for  $\omega_x$ , which was obtained along the  $z$ -axis at  $y = 1$  from figures 17(a) and 18(a). The DFT results are shown in figure 19 where the abscissa represents normalized wavelength ( $\lambda$ ) by cylinder diameter. For the natural shedding state at  $Re = 360$ , the dominant peak exists near  $\lambda = 1$ , as expected. In Case II, on the other hand, the magnitude of the peak near  $\lambda = 1$  is significantly diminished, but the dominant peak rather exists near  $\lambda = 3.5\pi/4 \simeq 2.7$  (Yoo *et al.* 2005). In order to investigate the dominant  $\lambda$  for Case II more clearly, we consider the axial energy spectrum (Poncet 2004) defined by

$$\|\hat{\mathbf{u}}\|_2^2 = \int_{\mathbb{R}^2} |\hat{\mathbf{u}}(x, y)|^2 dx dy, \quad (3.6)$$

with respect to  $\lambda$ , where  $\hat{\mathbf{u}}$  denotes the DFT of the velocity along the  $z$ -axis. Figures 20(a) and 20(b) show the axial energy spectra for Case II with respect to the normalized wavenumber  $2\pi/\lambda$  and normalized wavelength  $\lambda$  respectively. There is no significant resonance at  $t = 0.0$  (natural shedding state) as shown in figure 20(a). However, the resonance at  $2\pi/2.7 \simeq 2.3$  becomes stronger with time after forcing. The energy spectra in quasi-steady states ( $t = 87.5$  and  $t = 90.0$ ) exhibit strong resonance around  $\lambda = 2.7$ , as shown in figure 20(b). This long spanwise wavelength

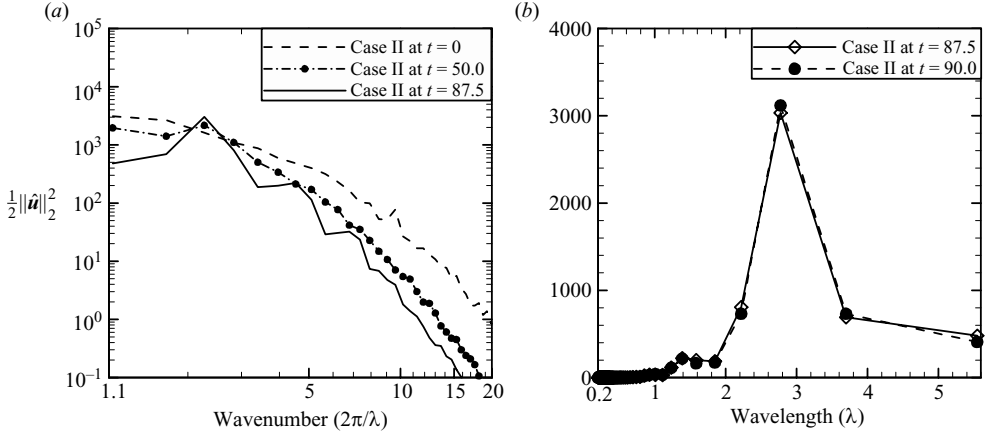


FIGURE 20. Axial energy spectrum for Case II. (a) Energy spectrum with respect to normalized wavenumber  $2\pi/\lambda$  in a logarithmic scale at  $t = 0.0$  (without forcing), 50.0 and 87.5 (quasi-steady states after forcing). (b) Energy spectrum with respect to wavelength  $\lambda$  in quasi-steady states at  $t = 87.5$  and  $t = 90.0$ .

of approximately 2.7 seems to be an extrapolated value from those corresponding to the spanwise wavelengths for mode-A instability of Williamson (1996a) (see figure 5).

From the examination of symmetry and spanwise wavelength,  $\omega_x$  contours in Case II in figure 18 are likely to originate from mode-A instability. Thus, we conclude that in Case II, mode A is the dominant instability in the near wake region since mode B-instability is suppressed due to the occurrence of vortex synchronization.

### 3.3.5. Saddle point in the braid shear layer

Suppression of mode-B instability at  $Re = 360$  can be explained by investigating the effect of vortex synchronization on the formation of saddle point. According to Williamson (1996b), for mode-B instability the streamwise vortex in the shear layer, perturbed by the previous braid vortices, is subject to tilting and stretching in proximity to the saddle point. This aspect was topologically investigated by Sung & Yoo (2003) using time-resolved PIV for the natural shedding state at  $Re = 360$ . They showed that the diverging separatrix of the saddle is aligned with the streamwise vortex filament, making the filament stretch along the diverging separatrix. During the process of vortex stretching, the surrounding fluid is advected to the saddle point along the converging separatrix, which produces large velocity fluctuations (Sung & Yoo 2003). Hence, by comparing the saddle point flows in the natural shedding and the vortex synchronization states, a clue for the suppression of mode-B instability may be found.

To compare the locations of the saddle points in the natural shedding and vortex synchronization states, figure 21 shows the streamlines and  $\omega_x$  contours in the  $x$ - $y$  plane at  $z = 2$ , superimposed on the  $\omega_z$  contours, where hollow circle and square represent vortex centre and saddle point, respectively. Figures 21(a) and 21(b) show streamlines and  $\omega_x$  contours for the natural shedding state at  $Re = 360$ . Likewise, figures 21(c) and 21(d) show streamlines and  $\omega_x$  contours for the Case II. Figure 21(a) is plotted after the quasi-steady states and figure 21(c) is plotted at 34.5 time units after the forcing, when they are at the same phase, i.e. when  $C_D$  curves reach the local minima. As shown in figures 21(a) and 21(c), the saddle point exists in the braid shear layer. Around this point, the braid shear layer perturbed by previous



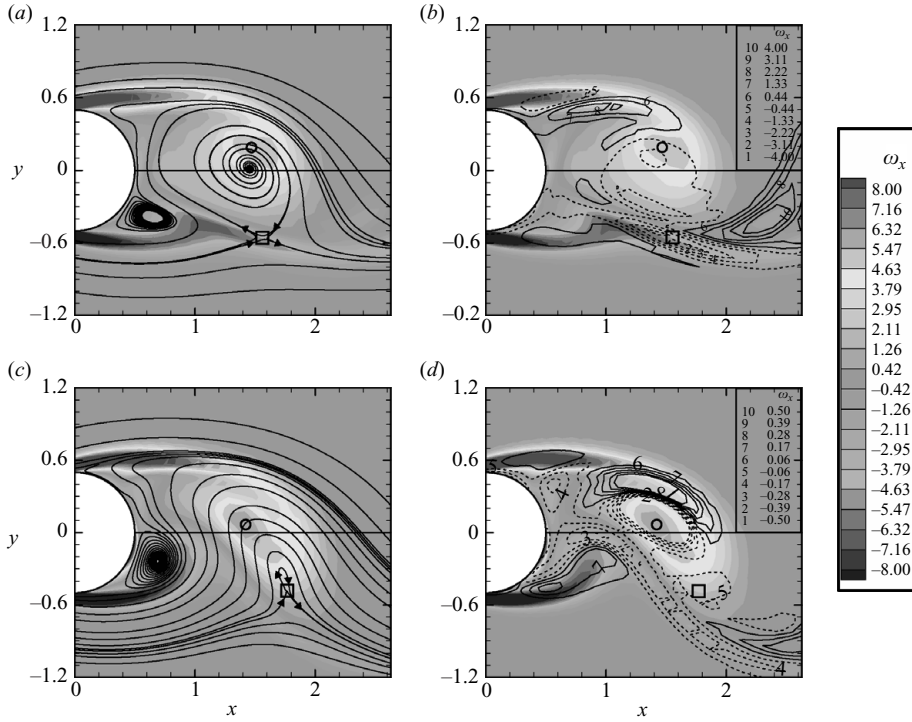


FIGURE 21. Comparison of (a) streamlines and (b)  $\omega_x$  contours in the  $x$ - $y$  plane at  $z=2$ , superimposed on  $\omega_z$  contours for the natural shedding state at  $Re=360$ , and likewise (c) streamlines and (d)  $\omega_x$  contours for the Case II, where hollow circle and square represent vortex centre and saddle point, respectively. Figure (a) is plotted at the same phase as figure (c) when  $C_D$  curves reach the local minima.

streamwise vortex is stretched along the diverging separatrix and strong  $\omega_x$  is induced by the velocity fluctuation due to the converging separatrix. We can see that the strong negative  $\omega_x$  in the braid shear layer is aligned with the diverging separatrix of the saddle, as shown in figures 21(a) and 21(b). However, for Case II, perturbed braid shear layer can not develop as a streamwise vortex since the saddle point is deviated from the braid shear layer. The deviated saddle point does not contribute to the generation of mode-B instability, inducing velocity fluctuation and stretching perturbed shear layer, so that the birth of the mode-B instability is suppressed for Case II.

The deviation of saddle point from the braid shear layer for Case II occurs because the strength and trajectory of the Kármán vortex is changed. The Kármán vortex becomes stronger with the vortex synchronization, as mentioned in §3.3.4. The magnitude of  $\omega_z$  around the centre of the Kármán vortex (local maximum of  $\omega_z = 6.3$ ) for Case II is higher than that (local maximum of  $\omega_z = 5.3$ ) for the natural shedding state, as shown in figure 21. Moreover, the coordinates of the vortex centres for the natural shedding state and for Case II are, respectively,  $(x, y) = (1.47, 0.19)$  and  $(1.42, 0.06)$ , so that the centre of the Kármán vortex for Case II is formed closer to the backside of the circular cylinder and the wake centreline than that of the natural shedding state. Because of the strengthened Kármán vortex and its modified trajectory, the braid shear layer is convected to the  $-y$  direction and further away from the saddle point.

#### 4. Conclusion

Direct numerical simulation is performed to investigate the vortex synchronization phenomena in the wake of a circular cylinder at the Reynolds numbers of 220 and 360, disturbed by the sinusoidal streamwise velocity perturbation.

The sinusoidal perturbation, which is superimposed to trigger vortex synchronization, is found to suppress the wake transition at  $Re = 220$  in such a manner that the vortex shedding frequency is modified from the natural shedding frequency to the frequency corresponding to two-dimensional laminar vortex shedding. For this reason, the base perturbation frequency for the vortex synchronization is not twice the natural shedding frequency but twice this hypothetical two-dimensional laminar vortex shedding frequency. In other words, the occurrence of vortex synchronization suppresses wake transition for mode A, so that the trough of the vortex synchronization regime of Griffin & Ramberg (1976) is formed around twice the two-dimensional laminar vortex shedding frequency, unlike the trough of natural vortex synchronization regime, which is formed around twice the natural shedding frequency.

The streamwise force balance of the mean wake bubble is investigated at both Reynolds numbers for the vortex synchronization state, on the extension of Kim *et al.* (2006). For the natural shedding state, the contribution of the Reynolds normal stress term is dominant at both Reynolds numbers. The contributions of respective terms are modified by vortex synchronization. That is, the contribution of the Reynolds shear stress force term to the force balance at  $Re = 220$  is negligible while its direction is reversed at  $Re = 360$ . This can be explained through the trajectory of the Kármán vortex, which is formed along the mean separating streamline inside the mean wake bubble at  $Re = 220$  while outside at  $Re = 360$ . Due to reversed direction of the Reynolds shear stress force term at  $Re = 360$ , the net pressure force acting on the mean wake bubble is increased, so that the contribution of pressure force is comparable with that of the Reynolds normal stress force. In contrast, at  $Re = 220$ , the Reynolds normal stress term is still dominant since the magnitude of pressure force term is hardly changed.

Vortex structure behind the circular cylinder is also modified due to the occurrence of vortex synchronization. At  $Re = 220$ , the flow behind the circular cylinder changes into two-dimensional laminar flow. On the other hand, at  $Re = 360$ , there exist streamwise vortex pairs although their strength is weaker than that of the natural shedding state. Dominant instability for this flow rather exhibits characteristics of mode-A instability with spanwise wavelength of approximately  $2.7D$ . From this, we conclude that mode-B instability is suppressed while mode-A instability become more dominant for the vortex synchronization state at  $Re = 360$ . The physical mechanism of suppression of the mode-B instability can be explained through the analysis of the saddle-point flow. The location of saddle point is deviated from the braid shear layer because of the strong Kármán vortex with the occurrence of vortex synchronization. This deviation of the saddle point suppresses the generation of mode-B instability in the braid shear layer, inducing velocity fluctuation and stretching perturbed shear layer.

This work has been supported by the BK21 Project, Mechanical Engineering Division, Seoul National University under the auspices of the Ministry of Education and Human Resources Development, Republic of Korea, and by Korea Institute of Science and Technology Information under ‘The Sixth and Seventh Strategic Supercomputing Support Program’.

## Appendix

Governing equations (2.1) in curvilinear coordinates  $(\xi, \eta, \zeta)$  (see figure 1a) take the form

$$\frac{\partial \mathbf{q}}{\partial t} + \frac{\partial(\mathbf{E} - \mathbf{E}_v)}{\partial \xi} + \frac{\partial(\mathbf{F} - \mathbf{F}_v)}{\partial \eta} + \frac{\partial(\mathbf{G} - \mathbf{G}_v)}{\partial \zeta} = 0, \quad (\text{A1})$$

where  $\mathbf{q} = J^{-1}[\rho, \rho u, \rho v, \rho w, E_T]^T$  is the solution vector,  $J$  is the Jacobian of the coordinate transformation,  $\mathbf{E}, \mathbf{F}, \mathbf{G}$  and  $\mathbf{E}_v, \mathbf{F}_v, \mathbf{G}_v$  are, respectively, convective and viscous flux vectors in each direction. For example,  $\mathbf{E} = J^{-1}(\xi_x \mathbf{e} + \xi_y \mathbf{f} + \xi_z \mathbf{g}) = J^{-1}[\rho U, \rho u U + \xi_x p, \rho v U + \xi_y p, \rho w U + \xi_z p, (E_T + p)U]^T$ , where  $\mathbf{e}, \mathbf{f}$  and  $\mathbf{g}$  are flux vectors in Cartesian coordinates and  $U = \xi_x u + \xi_y v + \xi_z w$  is the contravariant velocity component.

To overcome severe limitation on computational time step, fully implicit second-order Crank–Nicolson scheme is adopted. After linearization, (A1) takes the form

$$\left[ \mathbf{I} + \frac{\Delta t}{2} (\partial_\xi \mathbf{A} + \partial_\eta \mathbf{B} + \partial_\zeta \mathbf{C}) \right] \Delta \mathbf{q}^p = \mathbf{R}^{n,p}, \quad (\text{A2})$$

where  $\Delta \mathbf{q}^p = \mathbf{q}^{n+1} - \mathbf{q}^p$ ,  $\mathbf{A} = \partial(\mathbf{E} - \mathbf{E}_v)/\partial \mathbf{q}$ ,  $\mathbf{B} = \partial(\mathbf{F} - \mathbf{F}_v)/\partial \mathbf{q}$  and  $\mathbf{C} = \partial(\mathbf{G} - \mathbf{G}_v)/\partial \mathbf{q}$  are Jacobian matrices. Superscript  $p$  refers to the number of nonlinear subiterations during time advancement from the time level  $n$  to the new level  $(n + 1)$  with physical time step  $\Delta t$  in order to eliminate the linearization error. Thus, terms on the right hand side is given by  $\mathbf{R}^{n,p} = \mathbf{q}^n - \mathbf{q}^p - \frac{\Delta t}{2} [\partial_\xi (\mathbf{E} - \mathbf{E}_v)^n + \partial_\eta (\mathbf{F} - \mathbf{F}_v)^n + \partial_\zeta (\mathbf{G} - \mathbf{G}_v)^n + \dots]$ .

From past experience on numerical analysis, it is known that nonlinear iteration often diverges when the left-hand side of (A2) is discretized with low-order scheme while the right-hand side is discretized with high-order compact difference scheme. Thus, we adopt the fourth-order compact scheme for the left-hand side using the method proposed by Park *et al.* (2004), which is the extension of the method proposed by Ekaterinaris (1999). The key idea is to apply discrete weighted summation to (A2) with weights corresponding to the left-hand side of Pade scheme (see Ekaterinaris (1999) and Park *et al.* (2004) for more details). As shown by Ekaterinaris (1999), this scheme is linearly stable with arbitrary time step, although actual time step is limited by the nonlinearity of the problem and approximated Jacobians. For computational efficiency, the approximate factorization is introduced for the left-hand side of (A2) which is then solved by successive block tri-diagonal matrix inversion in direction-by-direction manner. The factorization error is also driven to zero by nonlinear iteration.

Recently, it is shown that the aliasing error leads to a significant consequence when kinetic energy conservation is violated because of the aliasing error (Park & Mahesh 2007). Thus, nonlinear terms in the right-hand side are written in skew-symmetric form to minimize the aliasing error (Park *et al.* 2004). For the momentum equation, the nonlinear term is written as

$$N_i = \frac{1}{2} \left( \frac{\delta \rho u_i u_j}{\delta x_j} + \rho u_j \frac{\delta u_i}{\delta x_j} + u_i \frac{\delta \rho u_j}{\delta x_j} \right), \quad (\text{A3})$$

where  $\delta/\delta x$  denotes numerical derivative. The aliasing error due to the first part (divergence form) and the second part (advective form) are of opposite sign so that their effects are cancelled by the summation (Kravchenko & Moin 1997). It is also shown (Blaisdell, Mansour & Reynolds (1991); Park & Mahesh (2007)) that the skew-symmetric form conserves kinetic energy in the inviscid incompressible limit. Therefore, the use of skew-symmetric form of convection term with high-order

compact scheme plays a similar role to the use of staggered grid with second-order scheme. However, it does not cure another source of numerical instability due to mesh non-uniformity. As analysed by You *et al.* (2006), mesh stretching and skewness also have adverse influence on the stability of second-order central difference. The instability becomes more serious with high-order compact Pade scheme, since disturbance/instability at any point instantly propagates to all the grid points of computational domain due to the global/implicit nature of Pade scheme, just like spectral method. On the other hand, disturbance remains local for explicit second-order scheme since the width of the stencil is just three grid points. That difference is why we need a filter for the current scheme. The main characteristic of adopted eighth-order compact filter is that it eliminates only very high frequencies near 2-delta wave (grid-to-grid oscillation). The validity of high-order filter associated with compact scheme is thoroughly investigated by Visbal and colleagues (see Visbal & Rizzetta 2002).

On the other hand, viscous terms on the right-hand side are discretized using staggered approach (Lele 1992; Nagarajan *et al.* 2003) to avoid the degradation of modified wavenumber characteristics due to the duplicate application of the first derivative. Terms in viscous flux vectors are defined at ‘half-grid shifted’ or staggered positions by using the following fourth-order difference and interpolation methods for an arbitrary function  $f$ :

$$f'_{i-1/2} + 22f'_{i+1/2} + f'_{i+3/2} = \frac{24}{\Delta} (f_{i+1} - f_i), \quad (\text{A4})$$

$$f^I_{i-1/2} + 6f^I_{i+1/2} + f^I_{i+3/2} = 4(f_{i+1} + f_i), \quad (\text{A5})$$

where the subscript denotes discrete indices,  $f'$  and  $f^I$  denote, respectively, derivative and interpolation, and  $\Delta$  is the grid spacing. Once viscous flux vectors are defined at staggered positions, the derivative of a flux is given by the following fourth-order compact scheme:

$$\begin{aligned} \frac{\partial}{\partial n_q} \partial_\xi \mathbf{E}_v|_{i-1} + 4 \partial_\xi \mathbf{E}_v|_i + \partial_\xi \mathbf{E}_v|_{i+1} \\ = \frac{15}{4\Delta\xi} (\mathbf{E}_v|_{i+1/2} - \mathbf{E}_v|_{i-1/2}) + \frac{3}{4\Delta\xi} (\mathbf{E}_v|_{i+3/2} - \mathbf{E}_v|_{i-3/2}). \end{aligned} \quad (\text{A6})$$

By using (A6) instead of (A4), the derivative of the viscous flux vector is computed without tri-diagonal matrix inversion because the left-hand side of (A6) corresponds to a weighted sum of discrete governing equations so that it is replaced by the right-hand side of (A6). Modified wavenumber analysis shows that this scheme significantly enhances resolution characteristics at high Reynolds numbers, and numerical results support analytic prediction.

Since there is no artificial viscosity in the present central differencing, the simulation can become easily unstable due to the amplification of various sources of numerical instability such as  $2\Delta$ -mode (odd-even decoupling), mesh non-uniformity, kinetic energy conservation and so on. To damp out such instabilities, a filtering technique is applied to the conservative variables using an eighth-order compact filter (Lele 1992; Visbal & Gaitonde 1999):

$$\alpha_f \bar{\mathbf{q}}_{i-1} + \bar{\mathbf{q}}_i + \alpha_f \bar{\mathbf{q}}_{i+1} = \sum_{n=0}^4 \frac{a_n}{2} (\mathbf{q}_{i-n} + \mathbf{q}_{i+n}), \quad (\text{A7})$$

where  $\alpha_f$  is the free parameter in the range of  $0 < |\alpha_f| \leq 0.5$ . The effect of the filter decreases as  $\alpha_f$  approaches 0.5 so that  $\alpha_f = 0.5$  corresponds to no filtering. The coefficients  $a_n$  are determined as the functions of  $\alpha_f$  by the Taylor series expansion. See Visbal & Gaitonde (1999) for their values. In this study, this filter is applied at every physical time step with  $\alpha_f = 0.495$ . It is shown in terms of energy spectra that this filter has negligible influence on the solution from the large eddy simulation of turbulent channel flow and turbulent flow past a cylinder at  $Re = 3900$  (Park *et al.* 2004).

## REFERENCES

- ARMSTRONG, B. J., BARNES, F. H. & GRANT, I. 1986 The effect of a perturbation on the flow over a bluff cylinder. *Phys. Fluids* **29**, 2095–2102.
- BALACHANDAR, S., MITTAL, R. & NAJJAR, F. M. 1997 Properties of the mean recirculation region in the wakes of two-dimensional bluff bodies. *J. Fluid Mech.* **351**, 167–199.
- BARBI, C., FAVIER, D. P., MARESCA, C. A. & TELIONIS, D. P. 1986 Vortex shedding and lock-on of a circular cylinder in oscillatory flow. *J. Fluid Mech.* **170**, 527–544.
- BEAUDAN, P. & MOIN, P. 1994 Numerical experiments on the flow past a circular cylinder at subcritical Reynolds number. *Tech. Rep.* TF-62. Thermosciences Division. Department of Mechanical Engineering, Stanford University.
- BLAISDELL, A., MANSOUR, N. N. & REYNOLDS, W. C. 1991 Numerical simulations of compressible homogeneous turbulence. *Tech. Rep.* TF-50. Thermosciences Division. Dept. of Mechanical Engineering, Stanford University.
- BREDE, M., ECKELMANN, H. & ROCKWELL, D. 1996 On secondary vortices in the cylinder wake. *Phys. Fluids* **8**, 2117–2124.
- EKATERINARIS, J. A. 1999 Implicit, high-resolution, compact schemes for gas dynamics and aeroacoustics. *J. Comput. Phys.* **156**, 272–299.
- FEY, U., KÖNIG, M. & ECKELMANN, H. 1998 A new Strouhal–Reynolds-number relationship for the circular cylinder in the range  $47 < Re < 2 \times 10^5$ . *Phys. Fluids* **10**, 1547.
- GRIFFIN, O. M. & HALL, M. S. 1991 Review - vortex shedding lock-on and flow control in bluff body wakes. *ASME J. Fluids Engng* **113**, 526–537.
- GRIFFIN, O. M. & RAMBERG, S. E. 1976 Vortex shedding from a cylinder vibrating in line with an incident uniform flow. *J. Fluid Mech.* **75**, 257–271.
- HENDERSON, R. D. 1997 Nonlinear dynamics and pattern formation in turbulent wake transition. *J. Fluid Mech.* **352**, 65–112.
- JIN, B. J., PARK, N. & YOO, J. Y. 2001 Large eddy simulation of boundary layer transition on the axial turbine blade by rotor induced wake. In *Proceedings of 2001 ASME Fluids Engineering Division Summer Meeting*, FEDSM2001-18195, New Orleans.
- KIM, J. & CHOI, H. 2005 Distributed forcing of flow over a circular cylinder. *Phys. Fluids* **17**, 033103.
- KIM, W., YOO, J. Y. & SUNG, J. 2006 Dynamics of vortex lock-on in a perturbed cylinder wake. *Phys. Fluids* **18**, 074103.
- KONSTANTINIDIS, E., BALABANI, S. & YIANNESKIS, M. 2003 The effect of flow perturbations on the near wake characteristics of a circular cylinder. *J. Fluids Struct.* **18**, 367–386.
- KRAVCHENKO, A. G. & MOIN, P. 1997 On the effect of numerical errors in large eddy simulations of turbulent flows. *J. Comput. Phys.* **131**, 310–322.
- KWON, K. & CHOI, H. 1996 Control of laminar vortex shedding behind a circular cylinder using splitter plates. *Phys. Fluids* **8**, 479–486.
- LELE, S. K. 1992 Compact finite difference schemes with spectral-like resolution. *J. Comput. Phys.* **103**, 16–42.
- MILLER, G. D. & WILLIAMSON, C. H. K. 1994 Control of three-dimensional phase dynamics in a cylinder wake. *Exp. Fluids* **18**, 26–35.
- MITTAL, R. & BALACHANDAR, S. 1997 On the inclusion of three-dimensional effects in simulations of two-dimensional bluff body wake flows. In *Proceedings of ASME Fluids Engineering Division Summer Meeting*, Vancouver, British Columbia, Canada. Available on CD-ROM only.

- NAGARAJAN, S., LELE, S. K. & FERZIGER, J. H. 2003 A robust high-order compact method for large eddy simulation. *J. Comput. Phys.* **191**, 392–419.
- PARK, N. & MAHESH, K. 2007 Analysis of numerical errors in large eddy simulation using statistical closure theory. *J. Comput. Phys.* **222**, 194–216.
- PARK, N., YOO, J. Y. & CHOI, H. 2004 Discretization errors in large eddy simulation: on the suitability of centred and upwind-biased compact difference schemes. *J. Comput. Phys.* **198**, 580–616.
- PERSILLON, H. & BRAZA, M. 1998 Physical analysis of the transition to turbulence in the wake of a circular cylinder by three-dimensional Navier–Stokes simulation. *J. Fluid Mech.* **365**, 23–88.
- PONCET, P. 2002 Vanishing of mode B in the wake behind a rotationally oscillating circular cylinder. *Phys. Fluids* **14**, 2021–2024.
- PONCET, P. 2004 Topological aspects of three-dimensional wakes behind rotary oscillating cylinders. *J. Fluid Mech.* **517**, 27–53.
- POSDZIECH, O. & GRUNDMANN, R. 2001 Numerical simulation of the flow around an infinitely long circular cylinder in the transition regime. *Theor. Comput. Fluid Dyn.* **15**, 121–141.
- ROSHKO, A. 1993 Perspectives on bluff body aerodynamics. *J. Wind Engng Ind. Aerodyn.* **49**, 79–100.
- SUNG, J. & YOO, J. Y. 2003 Near-wake vortex motions behind a circular cylinder at low Reynolds number. *J. Fluids Struct.* **17**, 261–274.
- TANIDA, Y., OKAJIMA, A. & WATANABE, Y. 1973 Stability of a circular cylinder oscillating in uniform flow or in a wake. *J. Fluid Mech.* **61**, 769–784.
- VISBAL, M. R. & GAITONDE, D. V. 1999 High-order-accurate methods for complex unsteady subsonic flows. *AIAA J.* **37**, 1231–1239.
- VISBAL, M. R. & RIZZETTA, D. P. 2002 Large-eddy simulation on curvilinear grids using compact differencing and filtering schemes. *ASME J. Fluids Engng* **124**, 836–847.
- WILLIAMSON, C. H. K. 1987 Three-dimensional transition in the near wake of a cylinder. *Bull. Am. Phys. Soc.* **32**, 2098.
- WILLIAMSON, C. H. K. 1992 The natural and forced formation of spot-like ‘vortex dislocations’ in the transition of a wake. *J. Fluid Mech.* **243**, 393–441.
- WILLIAMSON, C. H. K. 1996a Mode A secondary instability in wake transition. *Phys. Fluids* **8**, 1680–1682.
- WILLIAMSON, C. H. K. 1996b Three-dimensional wake transition. *J. Fluid Mech.* **328**, 345–407.
- WILLIAMSON, C. H. K. 1996c Vortex dynamics in the cylinder wake. *Annu. Rev. Fluid Mech.* **28**, 477–539.
- WILLIAMSON, C. H. K. & ROSHKO, A. 1990 Measurements of base pressure in the wake of a cylinder at low Reynolds numbers. *Z. Flugwiss. Weltraumforsch.* **14**, 38–46.
- YOO, J. Y., KIM, S. H. & BAE, J. H. 2006 Suppressed wake transition and vortex lock-on phenomena in a perturbed flow past a circular cylinder. *Bull. Am. Phys. Soc.* **51** (9), 127.
- YOO, J. Y., PARK, J. Y. & PARK, N. 2005 Direct numerical simulation of lock-on phenomenon in the wake of a circular cylinder. *Bull. Am. Phys. Soc.* **50** (9), 235.
- YOU, D., MITTAL, R., WANG, M. & MOIN, P. 2006 Analysis of stability and accuracy of finite-differencing schemes on a skewed mesh. *J. Comput. Phys.* **213**, 184–204.
- ZHANG, H.-Q., FEY, U. & NOACK, B. R. 1995 On the transition of the cylinder wake. *Phys. Fluids* **7**, 779–794.